PHYSICAL REVIEW B

SOLID STATE

THIRD SERIES, VOL. 2, NO. 11 1 DECEMBER 1970

# Infrared Absorption in Some II-VI Compounds Doped with Cr

J. T. VALLIN, G. A. SLACK, AND S. ROBERTS

*General Electric Research and Development Center, Schenectady, New York 12301*

AND

A. E. HUGHES*†

*Laboratory of Atomic and Solid State Physics, Cornell University, Ithaca, New York 14850*

(Received 15 July 1970)

The optical absorption spectra of substitutional $Cr^{2+}$ ($3d^4$) in single crystals of ZnS (cubic and mixed cubic-and-hexagonal), ZnSe, ZnTe, CdS, and CdTe have been measured for Cr concentrations of $10^{18}$–$10^{20}$ cm$^{-3}$ and at 2, 15, and 300°K in the wave-number range $5 \leq \bar{\nu} \leq 30\,000$ cm$^{-1}$. The room-temperature spectrum in the range $500 \leq \bar{\nu} \leq 30\,000$ cm$^{-1}$ is dominated by a broad absorption band at 5500 cm$^{-1}$ arising from the ${}^5T_2 \rightarrow {}^5E$ transition. These two levels originate from the crystal-field splitting of the ${}^5D$ free-ion ground state. At helium temperatures distinct lines appear on the low-energy side of the ${}^5T_2 \rightarrow {}^5E_2$ absorption band in all samples except for CdTe. These lines are associated with zero-phonon transitions and phonon-assisted transitions. As the temperature is increased, the relative intensities of some of the lines change due to the thermal population of low-lying levels belonging to the orbital $T_2$ state. In the case of ZnSe these levels have been studied in the far infrared in the range $5 \leq \bar{\nu} \leq 200$ cm$^{-1}$, both with and without a magnetic field. An interpretation of the results is made based on crystal-field theory with a strong, static, Jahn-Teller distortion of $E$ symmetry in the ${}^5T_2$ orbital ground state. There is little or no Jahn-Teller effect in the ${}^5E$ orbital excited state. The optical transitions exhibit a strong coupling to $E$-mode phonons of average energy $\sim$70 cm$^{-1}$.

## I. INTRODUCTION

The optical absorption of ions of the first transition series ($3d^n$) in adamantine compounds has been studied quite extensively in recent years.[1–35] There have been studies on Ti,[1] V,[2–4] Cr,[2,5–7] Mn,[2,8–13] Fe,[2,14–20] Co,[2,17,21–26] Ni,[2,22,26,23–29] and Cu.[2,19,22,30–35] It has been found in many cases that crystal-field theory[36,37] is a good starting point for giving an account of the energy levels of the $d$-shell electrons of these ions. However, it has also been shown[7,15,26,38,39] that when a detailed comparison between theory and experiment is made, it is important to treat the lattice as a dynamic system coupled to the electronic $d$ shell of the impurity ion. The first effect of this coupling is to produce phonon-assisted sidebands on the high-energy side of the zero-phonon optical-absorption lines. Such structure has been carefully studied for $Co^{2+}$, $Ni^{2+}$, and $Cu^{2+}$ in hexagonal ZnO,[26,32] for $Fe^{2+}$ in cubic ZnS, ZnSe, and CdTe,[15,18–20] and for $Mn^{2+}$ in cubic ZnSe.[11] Such careful high-resolution studies on "hexagonal" ZnS have been seriously bothered by uncertainties about polytypes.[15,34]

A second effect of this coupling to the lattice is to allow Jahn-Teller deformations at the impurity site. These Jahn-Teller effects can be either of the dynamic or static type.[38,39] We believe that the model of a static ⟨100⟩ axis distortion[39] in the ground state at the substitutional $Cr^{2+}$ impurity site can explain both the previous electron-spin-resonance results[40–43] as well as the present optical data. We will show that although the simple, undistorted cubic-crystal-field model can explain some of the general features of the spectra, this static distortion is needed to give a detailed interpretation.

## II. EXPERIMENTAL TECHNIQUE

The samples of ZnS, ZnSe, ZnTe, CdS, and CdTe that we used were all synthetic crystals. Melt-grown samples of "hexagonal" ZnS, hexagonal CdS, and cubic ZnSe and ZnTe were obtained from Eagle-Picher Industries.[44] The cubic ZnS and the CdTe were grown in this laboratory. The cubic ZnS was grown by Dr. J. Prener at 750°C using an iodine gas transport scheme. The CdTe was grown from the melt[45] by

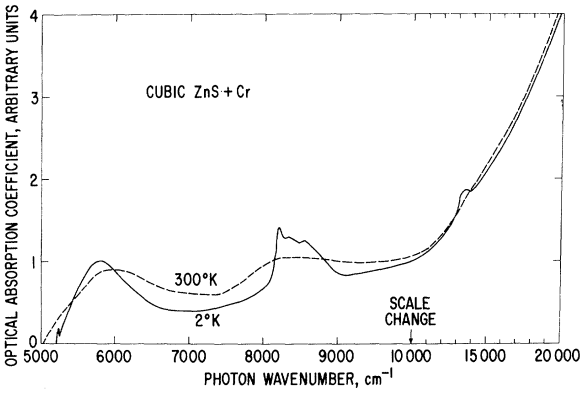


FIG. 1. Optical absorption coefficient versus photon wave number for a single crystal of cubic ZnS doped with Cr. The vertical scale has been adjusted to unity for the 2°K peak at $\bar{\nu}=5800$ cm$^{-1}$.

Dr. H. H. Woodbury. The Cr was introduced into some crystals, i.e., "hexagonal" ZnS and cubic ZnSe, during growth from the melt. For the others it was introduced by diffusion from an evaporated surface layer of metallic Cr. For the melt-grown crystals of ZnSe the Cr concentration was measured for some samples with an atomic absorption spectrophotometer.

The optical absorption in the far infrared was measured using two instruments. One was an interferometer[46] which covered the wave-number range $5\leq\bar{\nu}\leq100$ cm$^{-1}$. The second was a diffraction grating instrument[47] which covered $7\leq\bar{\nu}\leq200$ cm$^{-1}$. The higher-wave-number ranges were covered using a Beckman IR7[48] for $200\leq\bar{\nu}\leq4000$ cm$^{-1}$ and a Cary model 14[49] for $4000\leq\bar{\nu}\leq30\,000$ cm$^{-1}$. In all cases the percent transmission was measured with the light at normal

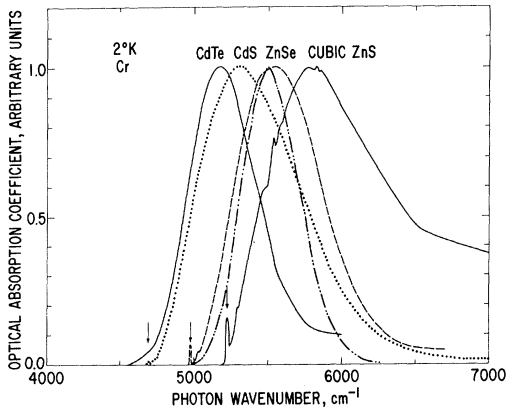


FIG. 2. Optical absorption coefficient versus photon wave number for four different Cr-doped crystals. The vertical scale has been adjusted to unity at the Cr absorption peak at 2°K. The dot-dot-dash curve for ZnSe is the expected shape based on model C.

or nearly normal incidence on a sample of thickness $t$. The optical absorption coefficient $\alpha$ was calculated from the expression

$$I=I_0(1-R)^2e^{-\alpha t}, \quad (1)$$

where $I_0$ is the incident light intensity, $I$ is the transmitted intensity, and $R$ is the single-surface reflection loss.

## III. EXPERIMENTAL RESULTS: NEAR INFRARED

### A. Cubic ZnS

We were able to diffuse Cr from an evaporated Cr metal film into this crystal at 1000°C in a sealed, fused silica tube. This temperature is sufficiently low so that the crystal remained cubic. The Cr concentration was high enough to allow us to measure the optical

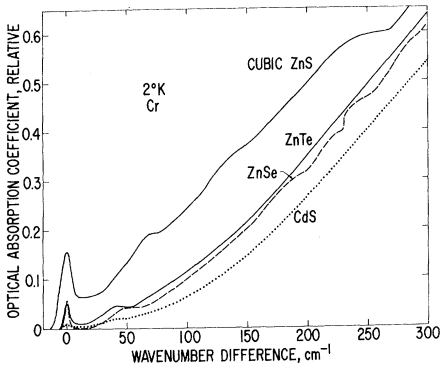


FIG. 3. Optical absorption coefficient versus photon wave-number energy differences above the zero-phonon line for four different Cr-doped crystals. The vertical scale, in relative units, has been adjusted to unity at the Cr absorption peak near $\bar{\nu}=5500$ cm$^{-1}$ at 2°K for all samples.

absorption spectrum. However, the Cr concentration in the 0.2-cm-thick sample is not uniformly distributed and is not known, so only relative values of the optical absorption coefficient are reported. We have arbitrarily assigned an absorption coefficient of unity to the absorption maximum at $\bar{\nu}=5800$ at 2°K. All other values are given relative to this peak. This same definition of optical-absorption coefficient in relative units is also used in many of the graphs.

The optical-absorption spectrum of $Cr^{2+}$ in cubic ZnS at 300 and 2°K for the range $5000\leq\bar{\nu}\leq20\,000$ cm$^{-1}$ is shown in Fig. 1. The 300°K curve shows two bands centered about $\bar{\nu}=6000$ and 8400 cm$^{-1}$. The 2°K curve shows these same bands with somewhat more structure, and a further band at $\bar{\nu}=13\,500$ cm$^{-1}$. The lowest-wave-number band at $\bar{\nu}=5800$ cm$^{-1}$ at 2°K is attributed[7] to the transition between the $^5T_2$ and $^5E$ levels derived from the $^5D$ ground state[50] of the free

TABLE I. Characteristics of the near-infrared absorption band of $Cr^{2+}$ in II-VI compounds.

| Crystal[a] | $\bar{\nu}$(peak, $cm^{-1}$)[b] 300°K | 2°K | $\bar{\nu}$(ZPL) ($cm^{-1}$) | ZPL width[c] ($cm^{-1}$) | Bandwidth[d] ($cm^{-1}$) | AR[e] ($10^{-2}$) | ZR[f] ($10^{-4}$) | First excited level ($cm^{-1}$) |
|---|---|---|---|---|---|---|---|---|
| ZnS | 6000 | 5800 | 5224±2 | 12 | 1035 | 16 | 18 | ··· |
| ZnS(hex.) | 6000 | 5780 | 5220±1[g] | 3.5 | 1035 | ··· | ··· | 6.0±0.3 |
| ZnSe | 5650 | 5525 | 4975±3 | 4.0 | 675 | 6.5 | 3.6 | 7.0±1.0 |
| ZnTe | 5620 | 5530 | 4994±2 | 5.5 | 570 | 5 | 4.6 | ··· |
| CdS(hex.) | 5500 | 5300 | 4686±2 | 9 | 750 | 1 | 1.1 | ··· |
| CdTe | 5280 | 5170 | 4700±100[h] | ··· | 540 | <1 | <1 | ··· |

[a] Crystals have the cubic sphalerite structure unless otherwise noted.
[b] Photon energy in wave numbers at the peak of the $^5T_2$-to-$^5E$ absorption band. The maximum shifts slightly with temperature.
[c] Width of the ZPL at 50% of maximum absorption.
[d] Width of the whole main absorption band at 50% of maximum absorption.
[e] AR is the absorption-coefficient ratio of peak of ZPL to peak of the main band.
[f] ZR is the integrated absorption intensity ratio of ZPL to that of the main band [see Eq. (3)].
[g] This is the ZPL for $Cr^{2+}$ in the cubic site in this polymorphic "hexagonal" ZnS.
[h] This is the estimated position of the ZPL, which was not seen.

ion. The assignments of the other two bands are uncertain. At 2°K the zero-phonon line, or ZPL, of this 5800-$cm^{-1}$ band occurs at $\bar{\nu}=5224\pm2$ $cm^{-1}$ in cubic ZnS and has a width (at one-half the maximum absorption coefficient) of $\Delta\bar{\nu}=12$ $cm^{-1}$. The height of the ZPL is 16% of the height of the main-band peak at $\bar{\nu}=5800$ $cm^{-1}$ at 2°K. This relationship is shown more clearly in Fig. 2. The integrated optical-absorption coefficient

$$I=\int\alpha(\bar{\nu})\,d\bar{\nu} \qquad (2)$$

can be computed in arbitrary units for both the ZPL and the main band at $\bar{\nu}=5800$ $cm^{-1}$. The ratio of these two for ZnS is

$$\mathrm{ZR}=I(\mathrm{ZPL})/I(\mathrm{main\ band})=18\times10^{-4}. \qquad (3)$$

This value is given in Table I.

In addition to the single ZPL the absorption band shows structure in the phonon-assisted absorption that extends over the range $5250\leq\bar{\nu}\leq7000$ $cm^{-1}$. These details are clearer in Figs. 2 and 3. The first peak in the phonon-assisted region occurs at $\bar{\nu}=5293$ $cm^{-1}$, or $\Delta\bar{\nu}=69$ $cm^{-1}$ above the ZPL (see Fig. 3). This and the other peaks in the phonon-assisted region and their tentative phonon assignments are listed in Table II. The energies of the lattice phonons in ZnS have been measured by Feldkamp *et al.*[51] These phonon energies for cubic ZnS are somewhat different from those given by Slack *et al.*[15] for cubic ZnS doped with $Fe^{2+}$.

### B. Hexagonal ZnS

No crystals of purely hexagonal ZnS were available. However, optical-absorption measurements were made on a melt-grown[44] crystal of ZnS into which Cr had been diffused at 1000°C in an argon ambient. A sample of melt-grown[44] ZnS containing Cr incorporated during growth was also studied. No significant differences were apparent in the two spectra. These samples were mixed polytypes of cubic and hexagonal ZnS. There are many ZPL's in these mixed-polytype crystals, as shown in Fig. 4. There are strong zero-phonon lines at $\bar{\nu}=5184$ and 5123 $cm^{-1}$ as well as at 5220 $cm^{-1}$. The 5220-$cm^{-1}$ line is believed to be due to $Cr^{2+}$ at Zn sites in cubic ZnS, while the other lines are probably associated with $Cr^{2+}$ in hexagonal ZnS. The two ZPL groups reported by Kelley and Williams[6] appear to be associated with these "hexagonal" sites. It does not seem worthwhile to present a detailed crystal-field model for these "hexagonal" sites. Similar extra ZPL's have been seen in mixed-polytype ZnS doped with[16,34] $Fe^{2+}$ or with $Cu^{2+}$. In Fig. 4 the optical-absorption coefficient is plotted relative to that of the peak at $\bar{\nu}=5800$ $cm^{-1}$ taken as unity. Thus it can be seen that

TABLE II. Phonon structure peaks at 2°K in the $Cr^{2+}$ absorption band in the near infrared and their probable assignments.

| Crystal | ZPL ($cm^{-1}$) | Phonon peak | $\Delta\bar{\nu}$[a] ($cm^{-1}$) | Probable assignment |
|---|---|---|---|---|
| Cubic ZnS | 5224 | 5293 | 69±2 | TA($L$) |
| | | 5354 | 130±6 | 2TA($L$) |
| | | 5475 | 250±5 | 4TA($L$) |
| | | 5538 | 314±4 | LO($X$) |
| | | 5574 | 350±4 | TO($L$) |
| | | 5825 | 601±3 | ? |
| | | 5855 | 631±6 | 2LO($X$) |
| ZnSe | 4975 | 5024 | 49±3 | TA($L$) |
| | | 5165 | 190±5 | 4TA($L$) or LA($X$) |
| | | 5193 | 218±5 | ? |
| | | 5210 | 235±5 | TO($L$) |
| | | 5255 | 280±5 | TO($L$)+TA($L$) |
| ZnTe | 4994 | 5033 | 39±2 | TA($L$) |
| CdS | 4686 | 4724 | 38±3 | TA($L$) |

[a] $\Delta\bar{\nu}$ = (phonon peak) −ZPL. The error limits given are based on an estimation of how accurately the difference $\Delta\bar{\nu}$ can be measured on the spectrometer chart. The peak energies are not very well defined (see Fig. 3).

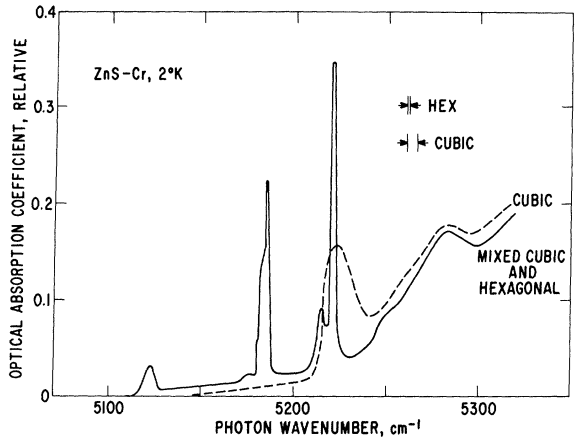


FIG. 4. Optical absorption coefficient versus photon wave number for Cr-doped cubic ZnS and "hexagonal" ZnS (which is really mixed cubic-and-hexagonal). The vertical scale, in relative units, has been adjusted to unity at the Cr absorption peak at $\bar{\nu}\cong 5800$ cm$^{-1}$ at 2°K for both samples. The "hexagonal" ZnS was not specifically oriented, and the light was unpolarized.

the integrated intensity $I$ of the three zero-phonon lines in the mixed-polytype sample is about the same as that of the one ZPL in the cubic sample. For both samples the width of the ZPL is limited by sample properties, not by the resolution of the instruments. The ZPL line for the mixed cubic- and-hexagonal sample at $\bar{\nu}=5220$ cm$^{-1}$ in Fig. 4, which has a half-width of $\Delta\bar{\nu}=3$ cm$^{-1}$, possesses a satellite at $\bar{\nu}=5214$ cm$^{-1}$ which is about $\frac{1}{5}$ as high. When this spectrum is studied at 20°K (not shown), the 5220-cm$^{-1}$ line decreases in height, while the 5214-cm$^{-1}$ line increases to become almost equal to the first line. Thus we see evidence for an excited state at $6.0\pm0.3$ cm$^{-1}$ above the ground state for Cr in the cubic sites in ZnS. Similar behavior is reported later for ZnSe.

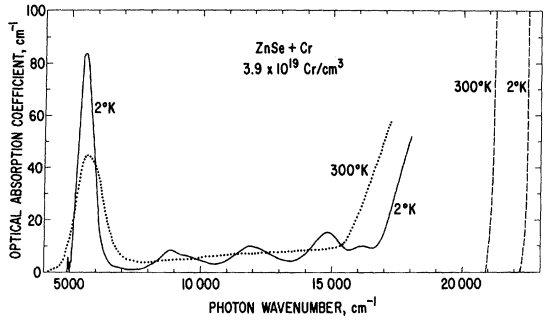


FIG. 5. Optical absorption coefficient versus photon wave number for Cr-doped ZnSe. The vertical scale is in absolute units. The two dashed lines on the right side give the absorption edge of pure, undoped ZnSe at the two temperatures.

### C. ZnSe

The optical-absorption coefficient $\alpha$ of melt-grown ZnSe single crystals[44] containing Cr was measured at 2 and 300°K. In these crystals the Cr was added prior to growth, and the Cr was distributed reasonably uniformly throughout the bulk of the samples. Thus absolute values of $\alpha$ were determined (see Fig. 5). At 300°K the main peak of the $^5T_2$-to-$^5E$ transition of $Cr^{2+}$ occurs at $\bar{\nu}=5650$ cm$^{-1}$. The variation of the magnitude of $\alpha$(peak) with the chemically measured total Cr concentration is shown in Fig. 6. The chemical determination does not differentiate between the different charge states of Cr. Thus Fig. 6 shows that the $Cr^{2+}$ concentration is proportional to the total Cr concentration. Electron-spin-resonance studies have

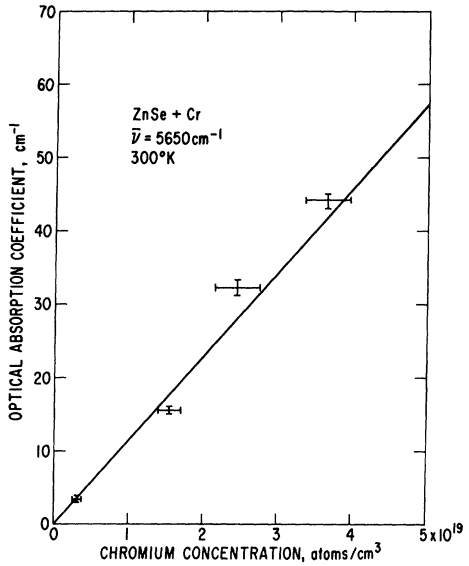


FIG. 6. Optical absorption coefficient of ZnSe in absolute units at the Cr absorption peak at $\bar{\nu}=5650$ cm$^{-1}$ versus the chemically measured total Cr concentration. The temperature is 300°K.

reported charge states of $+1$,[52–61] $+2$,[40–43,62] and $+3$[63] for Cr in II-VI compounds. From these studies the $Cr^{2+}$ ion appears to be the dominant charge state. It also appears to be the stable charge state in the compounds CrS, CrSe, and CrTe.[64] It seems reasonable to conclude that much and perhaps almost all (>95%) of the Cr is present as $Cr^{2+}$ ($3d^4$) for concentrations $\leq 4\times10^{19}$/cm$^3$. The $Cr^{1+}$ ions have been produced by illumination of the crystals containing $Cr^{2+}$ or by doping with trivalent ions such as $Al^{3+}$ or $Ga^{3+}$. The method of producing $Cr^{3+}$ ions[63] is unknown. We have annealed several crystals of Cr-doped ZnSe at 900°C in atmospheres of excess Zn and excess Se. No change was found in the shape, width, or magnitude of the ZPL or of the main band at $\bar{\nu}=5520$ cm$^{-1}$ (at 2°K)

after such treatments. Thus $Cr^{2+}$ is a stable charge state in ZnSe.

If we assume that all of the Cr is present as $Cr^{2+}$, then the integrated intensity $I$ [see Eq. (2)] yields a value for the oscillator strength of the $\bar{\nu}=5650$ cm$^{-1}$ band in ZnSe at 2°K of

$$f=(5\pm1)\times10^{-4}. \quad (4)$$

This value of $f$ for the whole band changes very little on going to 300°K. This value is less than that found in ZnS [6] or in CdS.[2] The origin of the other bands in Fig. at 2°K at $\bar{\nu}=8700$, 11 900, 14 700, and 16 400 cm$^{-1}$ is uncertain. These may be optical transitions to higher levels of the $3d^4$ configuration of $Cr^{2+}$.

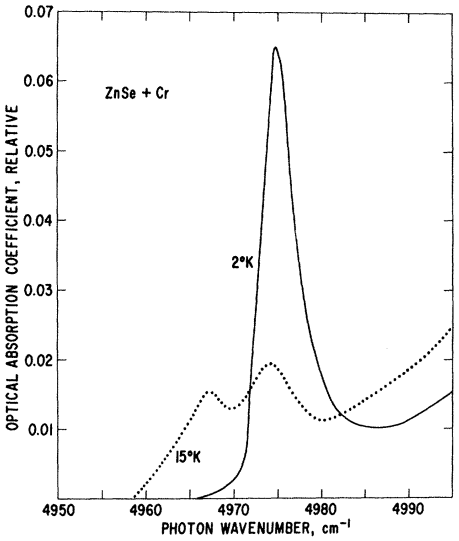


FIG. 7. Optical absorption coefficient versus photon wave number in the zero-phonon-line region of Cr-doped ZnSe. The "hot line" at $\bar{\nu}=4967$ cm$^{-1}$ at 15°K can be seen. The vertical scale has been adjusted to unity at the Cr absorption peak at $\bar{\nu}=5525$ cm$^{-1}$ at 2°K.

ZnSe has the same zinc-blende crystal structure that cubic ZnS has. For both crystals there is only one ZPL at 2°K. The ZPL is much narrower in ZnSe, being only 4.0 cm$^{-1}$ wide (see Table I), without any resolvable structure at an instrumental resolution of $\Delta\bar{\nu}=1.5$ cm$^{-1}$. The ratio in Eq. (3) for ZnSe is

$$ZR=3.6\times10^{-4}. \quad (5)$$

This value is somewhat less than that for cubic ZnS. Other parameters of the $Cr^{2+}$ in ZnSe absorption are listed in Table I.

An absorption curve for Cr-doped ZnSe was also run at 15°K with the sample immersed in liquid hydrogen. The ZPL now exhibits a "hot" band on its low-energy side at $\Delta\bar{\nu}=7\pm1$ cm$^{-1}$ below the main ZPL. These results are shown in Fig. 7, and are

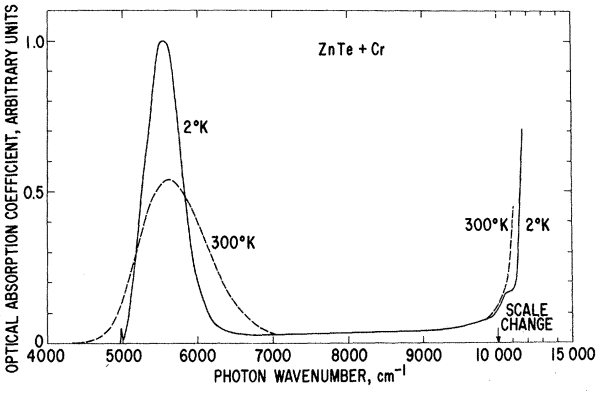


FIG. 8. Optical absorption coefficient versus photon wave number for Cr-doped ZnTe. The vertical scale has been adjusted to unity for the 2°K peak at $\bar{\nu}=5530$ cm$^{-1}$.

interpreted as the onset of an optical transition from a level located 7 cm$^{-1}$ above the ground state. The reduction of intensity of the 4975-cm$^{-1}$ ZPL with increasing temperature is also evident in Fig. 7. At 15°K it is reduced to (40±10)% of its intensity at 2°K. The presence of another level at $\bar{\nu}=7$ cm$^{-1}$ above the ground state has been verified by optical absorption measurements in the far infrared,[7] and will be treated in Sec. IV B.

In addition to the one ZPL at 2°K there are several peaks in the phonon-assisted region as shown in Figs. 2 and 3. The phonon energies are listed in Table II along with their tentative identifications. See Secs. VII H and VII I for a discussion of acoustic phonon energies in ZnSe.

### D. ZnTe

Samples of Cr-doped ZnTe were prepared by diffusion. The $\alpha$-versus-$\bar{\nu}$ curves at 2 and 300°K are shown

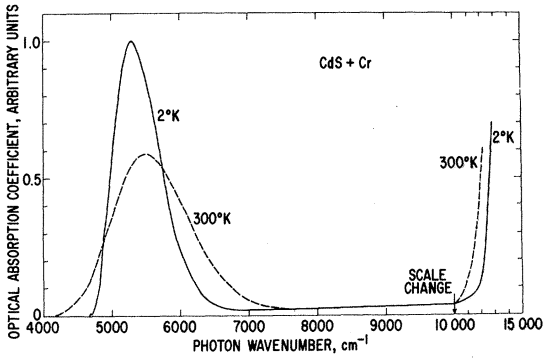


FIG. 9. Optical absorption coefficient versus photon wave number for Cr-doped CdS. The single-crystal sample was not specifically oriented, and the light was unpolarized. The vertical scale has been adjusted to unity for the 2°K peak at $\bar{\nu}=5300$ cm$^{-1}$.

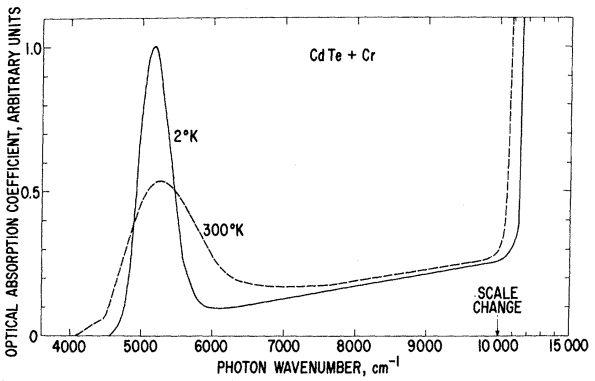


FIG. 10. Optical absorption coefficient versus photon wave number for Cr-doped CdTe. The vertical scale has been adjusted to unity for the 2°K peak at $\bar{\nu}=5170$ cm$^{-1}$.

in Fig. 8. The ZPL is at $\bar{\nu}=4994\pm2$ cm$^{-1}$ at 2°K, very close to the ZPL in ZnSe. Again ZnTe is cubic with the zinc-blende structure, and only one ZPL line with a width $\Delta\bar{\nu}=5.5$ cm$^{-1}$ is seen. The other parameters are given in Table I. The details of the phonon-assisted absorption are shown in Fig. 3. The only structure in the curve is at $\bar{\nu}=5033$ cm$^{-1}$ (see Table II).

### E. CdS

The optical-absorption curves of Cr diffused into wurtzite-structure CdS are shown in Fig. 9 for temperatures of 2 and 300°K. The ZPL is very weak, as can be seen in Figs. 3 and 9. The only phonon structure in the phonon-assisted region occurs at $\bar{\nu}=4724$ cm$^{-1}$. The various parameters derived from the absorption curve are given in Table I. The present curves for the $Cr^{2+}$ absorption peak near $\bar{\nu}=5500$ cm$^{-1}$ are in agreement with the previous work of Pappalardo and Dietz.[2] These authors did not, however, report any ZPL structure in their curves.

### F. CdTe

The $\alpha$-versus-$\bar{\nu}$ curves for Cr-doped CdTe prepared by diffusion are shown in Fig. 10. The general structure is the same as that found for the other II-VI compounds, and the $^5T_2$-to-$^5E$ band peaks at $\bar{\nu}=5280$ cm$^{-1}$ at 300°K. The main difference is that no ZPL could be seen in CdTe, which means its peak height at 2°K is probably less than 1% of the height of the phonon-assisted peak at $\bar{\nu}=5170$ cm$^{-1}$. From Fig. 3 and Table I we see that the relative height of the ZPL has been decreasing monotonically in the series cubic ZnS, ZnSe, ZnTe, and CdS. Now, in CdTe, it is undetectable.

## IV. EXPERIMENTAL RESULTS: FAR INFRARED

### A. ZnS

The optical absorption of a sample of polycrystalline melt-grown[44] "hexagonal" ZnS containing about $2\times10^{19}$/cm$^3$ of Cr was studied in the region $3\leq\bar{\nu}\leq110$ cm$^{-1}$. The main structure is a sharp absorption peak at $\bar{\nu}=70.0\pm0.5$ cm$^{-1}$ with a half-width of $\Delta\bar{\nu}\sim1$ cm$^{-1}$ and an absorption coefficient at the peak of $\alpha=0.7$ cm$^{-1}$ (see Fig. 11 and Table III). Since there is no intrinsic lattice absorption in undoped ZnS for $\bar{\nu}<110$ cm$^{-1}$, this is tentatively identified from the neutron scattering results[51] as a one-phonon TA($L$) absorption induced by the Cr impurity. No electronic transitions of $Cr^{2+}$ are expected in this energy range. The other broad absorption band covering $80\leq\bar{\nu}\leq110$ cm$^{-1}$ is probably due to other[51] TA phonons. No clearly identifiable absorption near $\bar{\nu}=6$ cm$^{-1}$ was seen.

### B. ZnSe

The optical absorption coefficient of pure ZnSe and of ZnSe samples doped with Cr and doped with Mn has been measured in the range $5\leq\bar{\nu}\leq4000$ cm$^{-1}$. These samples were grown from the melt by Eagle-Picher.[44] The results for $5\leq\bar{\nu}\leq200$ cm$^{-1}$ are shown in Fig. 12 at 4.2°K. In the range $200\leq\bar{\nu}\leq500$ cm$^{-1}$ the intrinsic lattice absorption was sufficiently strong so that no data were taken. See Aven *et al.*[65] and Mitra[66] for an approximate lattice absorption spectrum of ZnSe in this range. In the range $500\leq\bar{\nu}\leq4000$ cm$^{-1}$ some weak multiphonon lattice bands were seen at $\bar{\nu}=575$, 615, and 770 cm$^{-1}$ at room temperature with absorption coefficients at these peaks at 300°K of $\alpha\simeq1$ to 2 cm$^{-1}$. There are no discernible absorption peaks due to Cr in this region at 300°K.

The results in Fig. 12 show that the only absorptions that can be attributed to Cr at 4.2°K are the sharp absorption peak at $\bar{\nu}=7.4$ cm$^{-1}$ and a rather broad band between $40\leq\bar{\nu}\leq100$ cm$^{-1}$. This broad-band absorption is not present in pure ZnSe, but part of it does appear in $Mn^{2+}$-doped ZnSe (see Fig. 12). Comparable concentrations of Mn and Cr induce comparable values of the optical-absorption coefficient. From the selection rules for impurity-induced single-phonon transitions[67] we conclude that these bands are caused

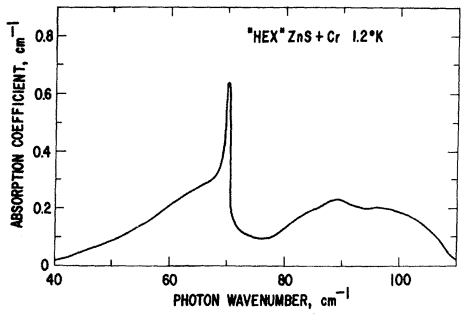


FIG. 11. Optical absorption coefficient in absolute units versus photon wave number in the far infrared for Cr-doped "hexagonal" ZnS (mixed cubic-and-hexagonal). The sample was not specifically oriented, and the light was unpolarized.

by one-phonon transitions. The assignments of the observed peaks to various critical point phonons are given in Table IV.

We conclude that the Cr produces one absorption peak at $\bar{\nu}=7.43$ cm$^{-1}$, the exact nature of which is still to be explained. The $\bar{\nu}=7.43$ cm$^{-1}$ line was measured with an interferometer type of spectrometer[46] using a liquid-He$^3$-cooled bolometer for increased sensitivity. The line width was deduced to be $\Delta\bar{\nu}\simeq 0.04$ cm$^{-1}$ after a suitable correction had been applied for the instrumental resolution of 0.06 cm$^{-1}$. From the known $Cr^{2+}$ concentration, the measured oscillator strength is $f=1.3\times10^{-9}$. The splitting of this line in a transverse magnetic field [see Fig. 5(b) of Ref. 20] was studied at 4.2°K with a grating spectrometer[47] at a resolution of $\Delta\bar{\nu}=0.3$ cm$^{-1}$ in the range $7\leq\bar{\nu}\leq10$ cm$^{-1}$. The line splits in a magnetic field, as shown in Fig. 13. The sample used was a multiply twinned sample, containing only zeroth-order and first-order twins.[68,69] The common [11$\bar{1}$] twinning axis was nearly normal to the sample surface and the two twinned orientations both possessed

TABLE III. Optical absorption bands of Cr-doped "hexagonal" ZnS in the far infrared.

| Wavenumber (cm$^{-1}$) | Probable assignment[a] | Comments |
|---|---|---|
| 6.0±0.3 | $Cr^{2+}$ | From near infrared only |
| 70 | TA($L$) | See Fig. 11 |
| 80–140 | Other TA | See Fig. 11 |

[a] We have given these identifications as if the sample were cubic ZnS instead of a mixed polytype.

a [011] axis nearly in the plane of the sample. The [011] was actually 10° out of the plane. Thus the $B$ vector was aligned nearly parallel to this common [011] axis. The sample contains equal concentrations of the three types of $Cr^{2+}$ centers having the three different contraction axes, i.e., [100], [010], and [001]. Thus a magnetic field in a [011] or [101] direction makes an angle of 45° with $\frac{2}{3}$ of the $Cr^{2+}$ centers and an angle of 90° with $\frac{1}{3}$ of them. This means the stronger absorption lines will be those for the 45° orientation. These are the points plotted in Fig. 13. The calculated curves in Fig. 13 are those for the 45° orientation, and are derived from the energy-levels-versus-magnetic-induction curves, given later, for a [001] axis center with the field in a [011] or [101] direction.

## V. EXPERIMENTAL RESULTS: ELECTRON SPIN RESONANCE

The $Cr^{2+}$ center has been studied previously in ZnSe[42,43] and CdS[40,41] by electron-spin-resonance

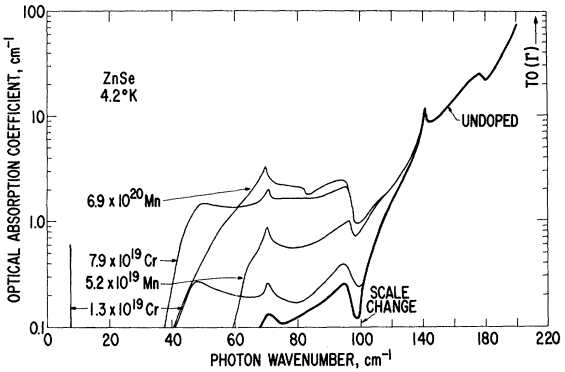


FIG. 12. Optical absorption coefficient in absolute units versus photon wave number in the far infrared for pure, Cr-doped, and Mn-doped ZnSe. The heavy solid line on the right-hand side is for undoped ZnSe. Only the Cr-doped samples were studied in the $5\leq\bar{\nu}\leq10$ cm$^{-1}$ region.

techniques. It was found that the Cr occupied a Zn site and had a charge state $Cr^{2+}$ ($3d^4$). The site is distorted along a ⟨001⟩ axis. The one exception to this model is provided by the work of Dorain and Locker,[62] who believed that the Cr is in an interstitial octahedral site in CdS. They have since stated in a private communication that, based on new results, the $Cr^{2+}$ is actually in a substitutional tetrahedral site in CdS. The comparison of the optical results for CdS in Fig. 2 with the other cubic crystals makes us also believe that the Cr in our CdS crystals is present as substitutional, tetrahedrally coordinated $Cr^{2+}$. Further evidence for the tetrahedral coordination of the $Cr^{2+}$ is the study[53,55,56] of the superhyperfine structure of the $Cr^{1+}$ centers generated from the

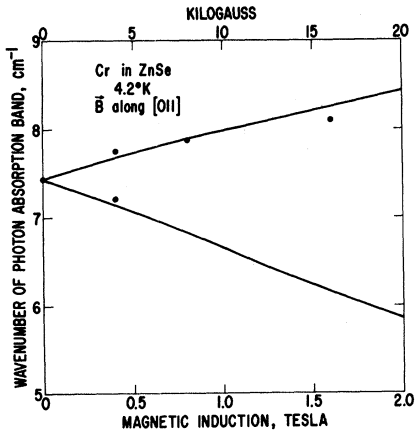


FIG. 13. Splitting of the $\bar{\nu}=7.43$ cm$^{-1}$ line of Cr-doped ZnSe in an applied magnetic field at 4.2°K. The field was applied nearly parallel to the [011] direction. The solid lines give the calculated behavior; the points give the observed absorption peaks.

TABLE IV. Optical absorption bands of pure and Cr-doped ZnSe in the far infrared.

| Photon wave number ($cm^{-1}$) | Probable assignment[a] | Impurity present[b] | Comments |
|---|---|---|---|
| 7.43±0.02 | $Cr^{2+}$ | Cr | Half-width = 0.04 $cm^{-1}$, electronic |
| 49±1 | TA($L$) | Cr | Impurity-induced one-phonon peak |
| 70.5±0.2 | TA($X$) | Cr, Mn, pure | Impurity-induced one-phonon peak |
| 96±1 | $A_2(K)$ | Cr, Mn, pure | Impurity-induced one-phonon peak |
| 141±1 | 2TA($X$) | Pure | Two-phonon peak |
| 176±1 | LA($L$)? | Pure | Impurity-induced one-phonon peak |

[a] The letters $K$, $L$, and $X$ refer to symmetry points in the Brillouin zone. At the $K$ point the TA branch has a lower $A_1$ and a higher $A_2$ value.
[b] The pure ZnSe was a melt-grown crystal obtained from Eagle-Picher Industries (Ref. 44). Typical analyses by a mass spectrograph of such crystals show that the dominant impurities are: oxygen $\sim 7\times10^{18}$ $cm^{-3}$, carbon $\sim 2\times10^{18}$ $cm^{-3}$, tellurium $\sim 1\times10^{18}$ $cm^{-3}$. Thus the total impurity content in the "pure" ZnSe may be about $1\times10^{19}$ $cm^{-3}$, which is sufficient to produce impurity-induced one-phonon peaks in the "pure" ZnSe.

$Cr^{2+}$ centers. The $Cr^{1+}$ centers were also found to be on undistorted substitutional sites replacing Zn or Cd.

The previous results[40–42] and some new results[43] for $Cr^{2+}$ in ZnTe are summarized in Table V. The quantities $g_{||}$, $g_\perp$, and $a$ are explained in Secs. VI D and VI E.

## VI. THEORY

The present results on the optical-absorption spectrum of $Cr^{2+}$ can be understood in first approximation by the application of crystal-field theory. Such models have been used previously.[1–39] However, as indicated in our first paper,[7] this basic model requires modification by the introduction of Jahn-Teller effects. This is the approach that is adopted here.

### A. General Hamiltonian

The Hamiltonian for noninteracting point defects in a host lattice can be written as

$$\mathcal{H}=\mathcal{H}_F+\mathcal{H}_{CF}+\mathcal{H}_{JT}+\mathcal{H}_{SO}++\mathcal{H}_{SS}+\mathcal{H}_B. \quad (6)$$

The first term, $\mathcal{H}_F$, is the free-ion term neglecting spin effects, $\mathcal{H}_{CF}$ represents the effect of the crystal field, $\mathcal{H}_{JT}$ causes the static Jahn-Teller distortion, $\mathcal{H}_{SO}$ is the spin-orbit coupling, $\mathcal{H}_{SS}$ is the spin-spin coupling, and $\mathcal{H}_B$ is the effect of the external magnetic field. In the case of transition-metal ions in II-VI compounds at substitutional sites the crystal-field splitting is typically smaller than the separation of the LS terms of the free ion ($\mathcal{H}_F > \mathcal{H}_{CF}$), but larger than the spin-orbit and spin-spin coupling ($\mathcal{H}_{CF} > \mathcal{H}_{SO}, \mathcal{H}_{SS}$).

### B. Cubic-Crystal-Field Theory

In simple cubic-crystal-field theory one assumes $\mathcal{H}_{JT}=C$. According to Hund's rules, the free-ion ground state for $Cr^{2+}$ ($3d^4$) is $^5D$. A crystal field $\mathcal{H}_{CF}$ of tetrahedral ($T_d$) symmetry will split this state by an amount defined as the crystal-field splitting $\Delta$ into an orbital doublet ($^5E$) and an orbital triplet ($^5T_2$), the latter being the ground state for $Cr^{2+}$. The spin-orbit and spin-spin coupling $\mathcal{H}_{SO}$ and $\mathcal{H}_{SS}$ will then split the degeneracies of the spin orbitals further, and the energy-level scheme obtained is given in Fig. 14. The corresponding eigenfunctions can be found in Ref. 20. In using Ref. 20 we note that $Cr^{2+}$ behaves as if $Dq>0$.

The $\mathcal{H}_{SO}$ and $\mathcal{H}_{SS}$ perturbations are given by[70–72]

$$\mathcal{H}_{SO}=+\lambda(\mathbf{L}\cdot\mathbf{S}),$$
$$\mathcal{H}_{SS}=-\rho[(\mathbf{L}\cdot\mathbf{S})^2+\tfrac{1}{2}(\mathbf{L}\cdot\mathbf{S})-\tfrac{1}{3}L(L+1)S(S+1)]. \quad (7)$$

In Fig. 14 the value of $K$ is given by

$$K(^5E)=(6\lambda^2/\Delta)-6\rho,$$
$$K(^5T_2)=(6\lambda^2/\Delta)+6\rho. \quad (8)$$

If $\rho=0$, then the two values of $K$ are equal; this was

TABLE V. Parameters of the $^5\hat{B}_2$ ground state derived from electron-spin-resonance studies.

| Crystal | $g_{||}$[a] | $g_\perp$ | $a$[b] ($cm^{-1}$) | $D$[c] ($cm^{-1}$) | Frequency (GHz) | $T$ (°K) | Ref. |
|---|---|---|---|---|---|---|---|
| CdS | 7.747 | 0 | 0.1503±0.0002 | −1.3±0.3 | 8, 9, 24 | 1.3–4.2 | 40, 41 |
| ZnSe | 7.837 | 0 | 0.024 | −2.48±0.01 | 9.2 | 1.2 | 42 |
| ZnTe | 7.92 | 0 | 0.13±0.01 | +2.30±0.02 | 14, 20 | 1.5–4.2 | 43 |

[a] For ZnTe the $g_{||}$ value for the $\hat{\Gamma}_5$ level is 3.96±0.02, while for the $\hat{\Gamma}_1\hat{\Gamma}_2$ nearly degenerate "doublet" it is 7.92±0.04. For the other crystals the $g_{||}$ value is for the $\hat{\Gamma}_1\hat{\Gamma}_2$ "doublet."
[b] For ZnTe the sign of $a$ was measured as $a=+0.13\pm0.01$ $cm^{-1}$.
[c] For ZnSe the value of $D$ was not found from EPR measurements, but was calculated from the far-infrared absorption at $\bar{\nu}=7.43$ $cm^{-1}$ ($|D|=\frac{1}{3}\bar{\nu}$).

the case considered in Ref. 20. In Fig. 14 we have used $\Delta>0$, $\lambda>0$, and $\rho>0$. The magnitudes of the splittings of the ${}^5T_2$ and ${}^5E$ states have been calculated by using the parameters $\Delta=|10|Dq=+4500$ cm$^{-1}$, $\lambda=+60$ cm$^{-1}$, and $\rho=+0.4$ cm$^{-1}$. The $\lambda$ and $\rho$ values are based on results for the free-ion $Cr^{2+}$. If we apply $\mathcal{H}_F+\mathcal{H}_{SO}+\mathcal{H}_{SS}$ of Eq. (6) to the free $Cr^{2+}$ ion and try to fit the observed[50] level structure of the ${}^5D$ ground state, the best fit is for $\lambda=+56.8$ cm$^{-1}$ and $\rho=+0.39$ cm$^{-1}$. The literature values for $\rho$ are $+0.42$ cm$^{-1}$ from Pryce[71] and $+0.12$ cm$^{-1}$ from Watson and Blume.[72] Trees[73] has shown that spin-orbit coupling between different LS terms provides an additional interaction having the same form as $\mathcal{H}_{SS}$ in Eq. (7). The spectroscopic value for $\rho$ of $+0.39$ cm$^{-1}$ thus represents the combined effect of these different LS terms and the true spin-spin interaction.[72] Thus we use this larger value of $\rho$. In the present model there are no covalency effects on $\lambda$, and the $\lambda$ values for the ${}^5T_2$ and ${}^5E$ states are assumed to be the same. The choice of $\Delta$ will be discussed later.

### C. Jahn-Teller Distortion

If $\mathcal{H}_{JT}\neq 0$, the theoretical treatment is more involved. We notice that the ESR results[40–43] for $Cr^{2+}$ indicate a tetragonally distorted lattice site, and do not agree with the model of Fig. 14, which is based on a cubic undistorted lattice site. We shall state here that the optical results do not agree very well either with the predictions of Fig. 14. The model that seems to fit best is where we have

$$\text{for } {}^5T_2 \text{ ground state, } \quad \mathcal{H}_{CF}>\mathcal{H}_{JT}\gg\mathcal{H}_{SO}>\mathcal{H}_{SS};$$

$$\text{for } {}^5E \text{ excited state, } \quad \mathcal{H}_{CF}\gg\mathcal{H}_{SO}>\mathcal{H}_{SS},\ \mathcal{H}_{JT}=0. \quad (9)$$

See Eq. (6) for the definitions. The justification for $\mathcal{H}_{JT}\cong 0$ in the ${}^5E$ state is based on the experimental results, and will be explained later. The next assumption we shall make is that $\mathcal{H}_{JT}$ gives rise to a static distortion in the orbital $T_2$ state. The ESR results indicate a distortion with a preferential [001] axis. This is in agreement with the predictions of Dunitz and Orgel,[74] who postulate a large $E$ distortion for $3d^4$ $Cr^{2+}$ in a tetrahedral site. The normal vibrational modes of a tetrahedron are given by Ballhausen[75] and Sturge.[39] The two $E$ distortions are $Q_\epsilon$ and $Q_\theta$ in Ham's[38] notation, or $Q_2$ and $Q_3$ according to Sturge,[39] and form a basis for a two-dimensional irreducible representation of $T_d$. The $Q_\theta$ distortion produces a compression or extension of the tetrahedral site along the twofold $z$ axis, the [001] axis, while the volume of the tetrahedron remains unchanged. Suitable linear combinations of $Q_\epsilon$ and $Q_\theta$ are needed to produce this equivalent distortion along either the [001] or the [010] axis. It is worthwhile to point out that the normal modes of a tetrahedron transform as $(A_1, E, T_2)$.

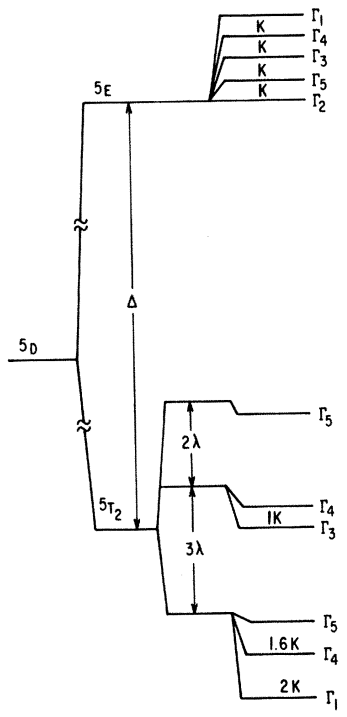


FIG. 14. Energy levels of $Cr^{2+}$ ($3d^4$) as predicted by crystal-field theory for an undistorted, substitutional cation site of $T_d$ symmetry. The ground state is the $\Gamma_1$ of ${}^5T_2$.

The $A_1$ distortion will not split either the $E$ or $T_2$ orbital states, the $E$ distortion will split both the $E$ and $T_2$ orbital states, while the $T_2$ will split only the orbital $T_2$ state.[39] Hence, if we are dealing with an $E$ distortion, we should expect splittings of both orbital states.

The most general Hamiltonian for a linear Jahn-Teller coupling consistent with the symmetry requirements is[38]

$$\mathcal{H}_{JT}=V_1(q_\theta\mathcal{E}_\theta+q_\epsilon\mathcal{E}_\epsilon)+V_2(q_\theta\mathcal{U}_\theta+q_\epsilon\mathcal{U}_\epsilon)+\tfrac{1}{2}\kappa(q_\theta^2+q_\epsilon^2)\mathcal{I}. \quad (10)$$

Here $V_1$ and $V_2$ are the coupling coefficients of the lattice to the orbital ${}^5T_2$ and ${}^5E$ states, respectively, and have the dimensions of energy. In general, $V_1\neq V_2$. The $q_\theta$ and $q_\epsilon$ are the dimensionless parameters which measure the magnitudes of the $Q_\theta$ and $Q_\epsilon$ lattice distortions. The $\mathcal{E}_\theta$ and $\mathcal{E}_\epsilon$ are electronic operators which operate on and only have matrix elements within the orbital $T_2$ wave functions. The $\mathcal{U}_\theta$ and $\mathcal{U}_\epsilon$ are similar, but only apply to the orbital $E$ wave functions. The $\frac{1}{2}(q_\theta^2+q_\epsilon^2)$ term is the elastic energy associated with the distortion, and $\mathcal{I}$ is the unit matrix.

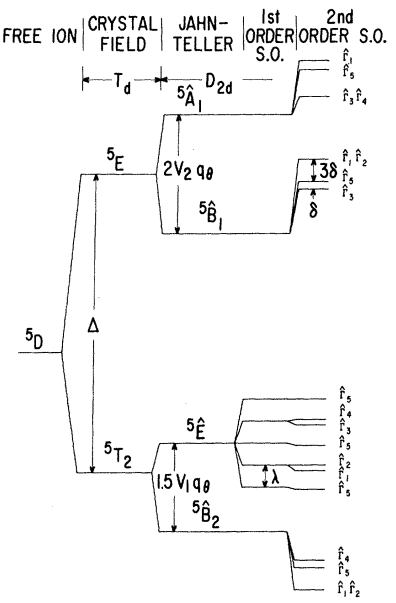


FIG. 15. Energy levels of $Cr^{2+}$ ($3d^4$) as predicted by crystal-field theory for a Jahn-Teller distorted, substitutional cation site of $D_{2d}$ symmetry. The ground state is the $\hat{\Gamma}_1\hat{\Gamma}_2$ of $^5\hat{B}_2$. The second-order spin-orbit splitting as shown also includes some first-order spin-spin splitting.

The orbital wave functions in $T_d$ symmetry are[20,36,38,70]

$$\begin{aligned}
^5E \text{ state:} \quad & |e\epsilon\rangle = (1/\sqrt{2})(Y_2^2 + Y_2^{-2}),\\
& |e\theta\rangle = +Y_2^0;\\
^5T_2 \text{ state:} \quad & |t_2\xi\rangle = +(i/\sqrt{2})(Y_2^1 + Y_2^{-1}),\\
& |t_2\eta\rangle = -(1/\sqrt{2})(Y_2^1 - Y_2^{-1}),\\
& |t_2\zeta\rangle = -(i/\sqrt{2})(Y_2^2 - Y_2^{-2}). \qquad (11)
\end{aligned}$$

In the absence of any static Jahn-Teller effect these states are separated in energy by an amount $\Delta$, with the $^5E$ state being higher for $Cr^{2+}$ (see Fig. 14). When $\mathcal{H}_{JT}$ in Eq. (10) is applied to the wave functions in Eq. (11), then the orbital doublet $^5E$ and the orbital triplet $^5T_2$ states each split into two states separated in energy at their respective equilibrium configurations by

$$\begin{aligned}
&\text{Splitting}(^5E) = +2V_2^2/\kappa = 4\mathcal{E}_{JT}(^5E),\\
&\text{Splitting}(^5T_2) = +3V_1^2/2\kappa = 3\mathcal{E}_{JT}(^5T_2). \qquad (12)
\end{aligned}$$

We have assumed the elastic constant $\kappa$ to be positive and to be the same for both states. The Jahn-Teller energies $\mathcal{H}_{JT}$ are not necessarily the same for both states, but become so if $V_1 = V_2$. The equilibrium values of $q_\theta$ and $q_\epsilon$ are, in general, different for the two orbital states. For the $^5E$ state the electronic energy levels versus $q$ are given by Fig. 6 of Sturge,[39] and the equilibrium occurs when

$$q_\theta^2 + q_\epsilon^2 = (V_2/\kappa)^2. \qquad (13a)$$

For the $^5T_2$ state the levels versus $q$ are given by Fig. 20 of Sturge.[39] There are three equivalent energy minima in this case at

$$\begin{aligned}
&q_\theta = +V_1/\kappa, \qquad q_\epsilon = 0,\\
&q_\theta = -V_1/2\kappa, \qquad q_\epsilon = +\sqrt{3}V_1/2\kappa,\\
&q_\theta = -V_1/2\kappa, \qquad q_\epsilon = -\sqrt{3}V_1/2\kappa. \qquad (13b)
\end{aligned}$$

These three minima correspond to static distortions along each of the three $\langle 100\rangle$ crystal axes.

If we arbitrarily set $q_\epsilon = 0$ and $q_\theta \neq 0$, then we have the case where the distortion is along the [001] axis. The local site symmetry of the $Cr^{2+}$ is then $D_{2d}$. This $q_\theta$ distortion will be convenient for graphically illustrating the behavior. In $D_{2d}$ symmetry the orbital $E$ and $T_2$ states of $T_d$ split into

$$\begin{aligned}
&^5E \rightarrow {}^5\hat{A}_1 + {}^5\hat{B}_1,\\
&^5T_2 \rightarrow {}^5\hat{B}_2 + {}^5\hat{E},
\end{aligned}$$

where

$$\begin{aligned}
&^5\hat{A}_1\text{: } |e\theta\rangle,\\
&^5\hat{B}_1\text{: } |e\epsilon\rangle,\\
&^5\hat{E}\text{: } |t_2\xi\rangle, |t_2\eta\rangle, \qquad (14)\\
&^5\hat{B}_2\text{: } |t_2\zeta\rangle.
\end{aligned}$$

Let us now define the energy differences:

$$\begin{aligned}
&\mathcal{E}_3 = \mathcal{E}(^5\hat{A}_1) - \mathcal{E}(^5\hat{B}_2),\\
&\mathcal{E}_2 = \mathcal{E}(^5\hat{B}_1) - \mathcal{E}(^5\hat{B}_2), \qquad (15)\\
&\mathcal{E}_1 = \mathcal{E}(^5\hat{E}) - \mathcal{E}(^5\hat{B}_2).
\end{aligned}$$

The carets indicate an irreducible representation of $D_{2d}$; those of $T_d$ have no carets. The splittings produced by $\mathcal{H}_{JT}$ of Eq. (10) with $q_\epsilon = 0$ and $q_\theta \neq 0$ combined with $\mathcal{H}_F + \mathcal{H}_{CF} + \mathcal{H}_{SO} + \mathcal{H}_{SS}$ are shown in Fig. 15, with both $V_2 q_\theta$ and $V_1 q_\theta$ as positive quantities. The energy differences are

$$\begin{aligned}
&\mathcal{E}_3 - \mathcal{E}_2 = 2V_2 q_\theta,\\
&\mathcal{E}_1 = 1.5V_1 q_\theta.
\end{aligned}$$

The EPR and far-infrared results tell us that the ground state is $^5\hat{B}_2$; hence $V_1 q_\theta > 0$. The sign of $q_\theta$ is positive if the $Cr^{2+}$ center has a compression along the [001] axis. A point-charge crystal-field model as well as some new ESR studies of the effects of external stress[43] give $q_\theta > 0$ for the $Cr^{2+}$ center. Hence we conclude that $V_1 > 0$.

In Fig. 16 we have neglected $\mathcal{H}_{SO}$, $\mathcal{H}_{SS}$, and $\mathcal{H}_B$ and we show the energy levels versus $q_\theta/q_0$ for various values of $V_2/V_1$. The equilibrium value of $q_\theta$ in the $^5\hat{B}_2$ ground state is just $q_0 = V_1/\kappa$. We now distinguish

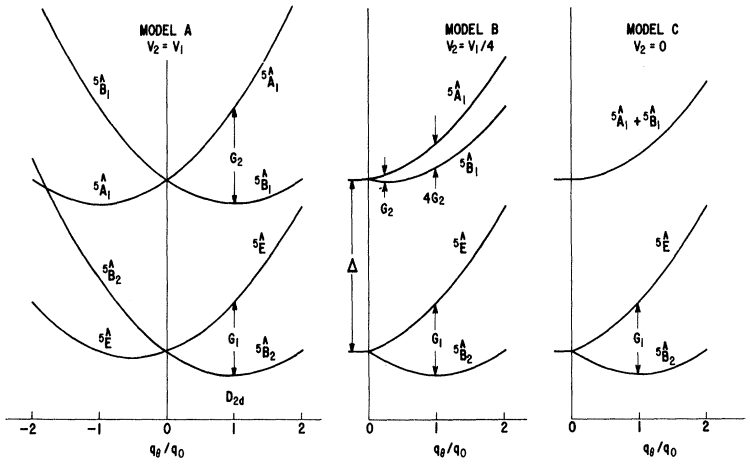


FIG. 16. Orbital energy levels of $Cr^{2+}$ ($3d^4$) in a substitutional cation site of $D_{2d}$ symmetry as a function of the tetragonal distortion. The equilibrium distortion in the ground state is $q_0$. The three models A–C all have the same lower two levels, but differ in the splitting of the upper third and fourth levels. The spin-orbit and spin-spin splittings are not included here. The two splitting parameters are $G_1=3\varepsilon_{JT}(^5T_2)=1.5V_1q_0$, $G_2=4\varepsilon_{JT}(^5E)$.

five different models for the $Cr^{2+}$ center as follows:

$$\begin{aligned} &\text{model A:} && V_2=V_1,\\ &\text{model B:} && V_2\cong\tfrac{1}{4}V_1,\\ &\text{model C:} && V_2\cong 0,\\ &\text{model D:} && V_2\cong-\tfrac{1}{4}V_1,\\ &\text{model E:} && V_2=-V_1. \end{aligned} \tag{16}$$

The energy-level structures for models E and D are the same as those for models A and B if we only interchange the labels of $^5\hat{A}_1$ and $^5\hat{B}_1$ in Fig. 16. The possible models where $|V_1|>|V_2|$ have been excluded for reasons which will be explained later. One of the tasks now is to see which of the models in Eq. (16) best fits the data.

One estimate of the ratio $V_2/V_1$ can be made from the point-charge model in which the $Cr^{2+}$ ion is surrounded by four point charges. In $T_d$ symmetry the crystal-field potential is just

$$V_{CF}=F(r)\{Y_4^0+(5/14)^{1/2}(Y_4^4+Y_4^{-4})\} \tag{17}$$

[see Eq. (A2) and Fig. 14 of Ref. 20]. Here the $Y_L^M$ are spherical harmonics.[36,37,70] When the site symmetry is lowered to $D_{2d}$ by a $Q_\theta$ distortion, other terms enter into $V_{CF}$. We designate these terms by a distortion potential

$$V_D=q_\theta G(r)[\{Y_2^0\}-(5\sqrt{5}/27)(r/d)^2\times\{Y_4^0-(7/10)^{1/2}(Y_4^4+Y_4^{-4})\}]. \tag{18}$$

Here $G(r)$ is some function of the radial distance $r$ of the $d$-shell electrons of the $Cr^{2+}$ ion from the Cr nucleus, $d$ is the distance from the Cr nucleus to any one of the four surrounding anions, and $q_\theta$ is the dimensionless quantity which measures the linear shift of the four anions away from their normal positions in $T_d$ symmetry. The $V_D$ term is zero if $q_\theta=0$. The sign of $V_D$ changes with the sign of $q_\theta$. Notice that both of the terms in curly brackets in Eq. (18) are orthogonal to the curly-bracket term in Eq. (17). An expression similar to Eq. (18) has been given by Ballhausen[75] on p. 100, but his result lacks the orthogonality condition. The energy differences with respect to the free-ion $^5D$ level of the electronic levels of $Cr^{2+}$ as given by the wave functions in Eq. (14) are calculated by applying $V_{CF}$ and $V_D$ from Eqs. (17) and (18). The results are

$$\begin{aligned} \varepsilon(^5\hat{A}_1)&=+0.6\Delta+2Ds-3Dt,\\ \varepsilon(^5\hat{B}_1)&=+0.6\Delta-2Ds+3Dt,\\ \varepsilon(^5\hat{E})&=-0.4\Delta+Ds+2Dt,\\ \varepsilon(^5\hat{B}_2)&=-0.4\Delta-2Ds-4Dt. \end{aligned} \tag{19}$$

The $\Delta$ term comes from $V_{CF}$, while the $Ds$ and $Dt$ terms come from the first and second curly-bracket terms in $V_D$, respectively. A positive value of $Ds$ arises from a contraction of the tetrahedron along the [001] axis; i.e., $q_\theta>0$, in agreement with Dunitz and Orgel.[74] From this point-charge model we have

$$\begin{aligned} &^5E: && \varepsilon_3-\varepsilon_2=2V_2q_\theta=4Ds-6Dt,\\ &^5T_2: && \varepsilon_1=1.5V_1q_\theta=3Ds+8Dt. \end{aligned} \tag{20}$$

From Eq. (18) the ratio $Dt/Ds$ is given by

$$Dt/Ds=[10(r/d)^2]/27 \tag{21}$$

from a point-charge model. Using an estimate of $r^2$ for $Cr^{2+}$ $3d^4$ of $5.0\times10^{-17}$ cm$^2$ based on calculations of Tucker,[76] we compute for ZnSe that

$$Dt/Ds=0.0077. \tag{22}$$

Hence we neglect $Dt$ compared to $Ds$, and arrive at

$$\begin{aligned} \varepsilon_3&=\Delta+4Ds,\\ \varepsilon_2&=\Delta,\\ \varepsilon_1&=3Ds \end{aligned} \tag{23}$$

and

$$\mathcal{E}_3-\mathcal{E}_2=2V_2q_\theta=4Ds,$$
$$\mathcal{E}_1=1.5V_1q_\theta=3Ds. \quad (24)$$

Equation (24) shows that a point-charge model gives $V_1>0$, since $q_\theta>0$ means $Ds>0$. The other result of the model is that

$$V_2=V_1>0$$
or
$$\mathcal{E}_{JT}(^5E)=\mathcal{E}_{JT}(^5T_2)>0 \quad (25)$$

[see Eq. (12)]. These results correspond to model A of Eq. (16).

We realize that we have neglected any covalency effects in using this point-charge model. Since we are dealing with II-VI compound semiconductors, this is a great and probably unjustified assumption. However, the model does show how $V_1$ and $V_2$ are related in a simple, special case. To calculate $V_2/V_1$ for a realistic, covalent model of the crystal is beyond the scope of this paper.

### D. Spin-Orbit and Spin-Spin Coupling

In the following discussion we shall assume that

$$\Delta>3\mathcal{E}_{JT}(^5T_2)\gg\lambda>D. \quad (26)$$

Then we can apply the $\mathcal{H}_{SO}$ and $\mathcal{H}_{SS}$ perturbations of Eq. (7) to the spin-orbit product wave functions. Since we are in the high-spin state of $3d^4$, we have $S=2$, and the spin-wave functions are $|S\epsilon\rangle$, $|S\theta\rangle$, $|S\xi\rangle$, $|S\eta\rangle$, and $|S\zeta\rangle$, similar to Eq. (11). There are a total of $(2L+1)\times(2S+1)=25$ product wave functions now.[20] We shall not list all of them, but will point out that they belong to the following irreducible representations of $D_{2d}$ symmetry:

| Orbital state | Spin-orbit wave functions |
|---|---|
| $^5\hat{A}_1$ | $\hat{\Gamma}_1+\hat{\Gamma}_3+\hat{\Gamma}_4+\hat{\Gamma}_5$ |
| $^5\hat{B}_1$ | $\hat{\Gamma}_1+\hat{\Gamma}_2+\hat{\Gamma}_3+\hat{\Gamma}_5$ |
| $^5\hat{E}$ | $\hat{\Gamma}_1+\hat{\Gamma}_2+\hat{\Gamma}_3+\hat{\Gamma}_4+3\hat{\Gamma}_5$ |
| $^5\hat{B}_2$ | $\hat{\Gamma}_1+\hat{\Gamma}_2+\hat{\Gamma}_4+\hat{\Gamma}_5$ (27) |

$\hat{\Gamma}_1$, $\hat{\Gamma}_2$, $\hat{\Gamma}_3$, and $\hat{\Gamma}_4$ are one-dimensional representations and $\hat{\Gamma}_5$ is two dimensional. The character tables for the $T_d$ and $D_{2d}$ groups can be found in Tinkham[77] and in Koster *et al.*[78] The correct product wave functions for each of these irreducible representations can be found from the tables of Koster *et al.*[78–80] Note that as in Ref. 15 we use Mulliken's notation for orbital states and Bethe's for spin-orbit product states.

The relative energies of the 19 different levels of Eq. (27) depend on the values of $\Delta$, $\mathcal{E}_{JT}(^5T_2)$, $\mathcal{E}_{JT}(^5E)$, $\lambda$, and $\rho$. The approximate results for ZnSe are shown in Fig. 15. Notice that only the orbital $^5\hat{E}$ levels show a first-order spin-orbit splitting, and this results in five levels separated by successive energies $\lambda$. Second-order spin-orbit splittings also occur in the $^5\hat{E}$ state as shown and remove the $\hat{\Gamma}_1-\hat{\Gamma}_2$ and $\hat{\Gamma}_3-\hat{\Gamma}_4$ accidental degeneracies. The orbital singlet states $^5\hat{A}_1$, $^5\hat{B}_1$, and $^5\hat{B}_2$ only split in second order under $\mathcal{H}_{SO}$ and in first order under $\mathcal{H}_{SS}$. Each of these states can be considered as a spin $S=2$ state with a fixed orbital wave function. For $^5\hat{B}_2$ the orbital wave function is $|t_2\zeta\rangle$ and the product wave functions are

$$\hat{\Gamma}_1:|t_2\zeta,\ S\zeta\rangle,$$
$$\hat{\Gamma}_2:|t_2\zeta,\ S\epsilon\rangle,$$
$$\hat{\Gamma}_3:|t_2\zeta,\ S\theta\rangle, \quad (28)$$
$$\hat{\Gamma}_5:|t_2\zeta,\ S\xi\rangle,\ |t_2\zeta,\ S\eta\rangle.$$

Contributions to these wave functions of order $\lambda/3\mathcal{E}_{JT}(^5T_2)$ and $\lambda/\Delta$ from mixing with other orbital states have been neglected. The second-order effect of $\mathcal{H}_{SO}$ and first-order effect of $\mathcal{H}_{SS}$ is to split the spin states in energy according to

$$\text{energy}=+D[(S_z)^2-\tfrac{1}{3}S(S+1)]. \quad (29)$$

The value of $D$ is a meaningful quantity for the $^5\hat{B}_2$ state, and is meaningful for $^5\hat{A}_1$ and $^5\hat{B}_1$ only if $^5\hat{A}_1$ and $^5\hat{B}_1$ are not degenerate. This means $V_2\neq0$ in Eq. (16); i.e., model C is excluded. The value of $D$ has been computed for models A, B, D, and E to be

$$D(^5\hat{A}_1)=-[3\lambda^2/(\mathcal{E}_3-\mathcal{E}_1)]+3\rho,$$
$$D(^5\hat{B}_1)=+4\lambda^2/\mathcal{E}_2-[\lambda^2/(\mathcal{E}_2-\mathcal{E}_1)]-3\rho, \quad (30)$$
$$D(^5\hat{B}_2)=-4\lambda^2/\mathcal{E}_2-\lambda^2/\mathcal{E}_1-3\rho,$$

where $\mathcal{E}_3$, $\mathcal{E}_2$, and $\mathcal{E}_1$ are given in Eq. (15). Note that in Eq. (30) the contribution of the $\rho$ term is significant because the splittings are so small. Equation (29) shows that when $D>0$ the $S_z=0$ level is lowest, but when $D<0$ the $S_z=\pm2$ levels are lowest. When $D=0$, then all five spin levels have the same energy. From Eqs. (12), (15), and (30) we see that $D(^5\hat{A}_1)<0$ and $D(^5\hat{B}_1)>0$, but that $D(^5\hat{B}_2)$ is variable depending on the relative magnitudes of $\mathcal{E}_2$ and $\mathcal{E}_1$. Since $^5\hat{B}_2$ is the ground state of the system, this can have important consequences. Figure 15 has been drawn for ZnSe, where, experimentally, $D(^5\hat{B}_2)<0$.

In Eq. (29) the $S_z=+2$ level has the same energy as the $S_z=-2$. This is not completely true; there are higher-order effects of $\mathcal{H}_{SO}$ and $\mathcal{H}_{SS}$ which split this accidental degeneracy. For the $^5\hat{B}_2$ ground state the $\hat{\Gamma}_1$-to-$\hat{\Gamma}_2$ energy difference is given to order $\lambda^4$ and $\rho\lambda^2$ by

$$a=\mathcal{E}(\hat{\Gamma}_2)-\mathcal{E}(\hat{\Gamma}_1)=36\lambda^2[\lambda^2+\rho(2\mathcal{E}_1+\mathcal{E}_3)]/\mathcal{E}_1^2\mathcal{E}_3. \quad (31)$$

### E. Applied Magnetic Fields

If we apply an external magnetic field, we will remove the remaining degeneracies. Consider the effect of the perturbation

$$\mathcal{H}_B=\mu_B(\mathbf{L}+2\mathbf{S})\cdot\mathbf{B}, \tag{32}$$

where $\mu_B$ is the Bohr magneton and $\mathbf{B}$ is the magnetic induction. We shall only consider the case of the ${}^5\hat{B}_2$ state. First let the magnetic-field splittings be small compared to $D$ [see Eq. (30)]. The results for $\mathbf{B}$ parallel to the [001] distortion axis are shown in Fig. 17. The wave functions of the $S_z=\pm 2$ states are, respectively,

$$\Psi_{(\pm)}=(1/\sqrt{2})[|\, t_2\zeta,\ S\epsilon\rangle \pm |\, t_2\zeta,\ S\zeta\rangle] \tag{33}$$

and are mixtures of the $\hat{\Gamma}_1$ and $\hat{\Gamma}_2$ wave functions. The effective $g$ values are dependent on the spin-orbit mixing of the wave functions of the ${}^5\hat{B}_1$ state into the ${}^5\hat{B}_2$ ground state. The results are

$$\begin{aligned} g_{||}(\hat{\Gamma}_1,\hat{\Gamma}_2)&=8[1-(4\lambda/\Delta)],\\ g_{||}(\hat{\Gamma}_5)&=4[1-(4\lambda/\Delta)],\\ g_{\perp}(\hat{\Gamma}_1,\hat{\Gamma}_2)&=g_{\perp}(\hat{\Gamma}_5)=0. \end{aligned} \tag{34}$$

The quantity $g_{||}$ is obtained when $|\mathbf{B}|=B_z$ and $g_\perp$ when $\mathbf{B}$ is perpendicular to the $z$ axis, i.e., the distortion axis of the $Cr^{2+}$ center.

When the magnetic field becomes sufficiently large so that $g\mu_B\mathbf{B}$ is comparable to $D$ and when $\mathbf{B}$ has $B_x$ or $B_y$ components, then the energy levels versus magnetic induction have to be found by solving a $5\times 5$ determinant. The results for several directions of $\mathbf{B}$ are shown in Fig. 18. The distortion axis of the $Cr^{2+}$ center is chosen, as before, as the [001] axis. Notice that the lowest energy of all occurs with $\mathbf{B}=B_z$ only. Some interesting possibilities of reorienting the centers by applied magnetic fields at low temperatures are apparent.

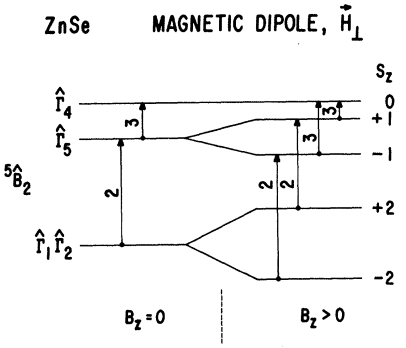


FIG. 17. Levels of the ${}^5\hat{B}_2$ ground-state manifold in zero and nonzero applied magnetic fields. The vertical arrows give the allowed magnetic dipole optical transitions for the case where $\mathbf{H}$ for the photons is perpendicular to the [001] distortion axis of the center. The relative intensities REI of the various transitions are given by the numbers on the vertical arrows [see Eq. (35)].

### F. Optical Transitions: Models A, B, D, and E

There are allowed optical transitions between the various spin-orbit levels. We can calculate these for models A, B, D, and E of Eq. (16). Within the ${}^5\hat{B}_2$ state the optical transitions are all in the far-infrared region. The only strong transitions are magnetic dipole in origin. The only allowed ones are those between the $(\hat{\Gamma}_1, \hat{\Gamma}_2)$ level and the $\hat{\Gamma}_5$, and also between $\hat{\Gamma}_5$ and $\hat{\Gamma}_4$. These are only allowed when the magnetic vector $\mathbf{H}$ of the light beam is perpendicular to the $z$ distortion axis of the $Cr^{2+}$ center. The relative intensities (REI) for plane-polarized light with $H_\perp$ are 2 and 3, as given in Fig. 17. In Fig. 17 we have given the relative intensity as

$$\text{REI}=|\,\langle\Psi_f|\,\text{operator}\,|\Psi_i\rangle\,|^2, \tag{35}$$

where we use the magnetic dipole operator between the initial state $\Psi_i$ and the final state $\Psi_f$. For levels possessing degeneracy we have summed over the final and averaged over the initial states. It can be seen that only the $\delta S_z=\pm 1$ transitions are allowed.

In the visible and near-infrared region the electric dipole transitions are the dominant ones, and we are interested in the allowed transitions from ${}^5B_2$ to ${}^5\hat{E}$, ${}^5\hat{B}_1$, and ${}^5\hat{A}_1$. The absolute intensities of electric dipole transitions are difficult to calculate because the intensities depend on the amount of wave-function mixing from other free-ion states, and on the poorly known radial part of the wave functions. The relative intensities were calculated using the equivalent operators[78,81] in $D_{2d}$ symmetry,

$$\begin{aligned} &\hat{\Gamma}_4,\ E_{||}\colon L_xL_y+L_yL_x,\\ &\hat{\Gamma}_5,\ E_\perp\colon L_zL_x+L_xL_z,\ L_zL_y+L_yL_z. \end{aligned} \tag{36}$$

Here $E_{||}$ and $E_\perp$ mean that the electric vector of the plane-polarized light beam is either parallel or perpendicular to the $z$ distortion axis of the $Cr^{2+}$ center. The electric dipole transitions from ${}^5\hat{B}_2$ to ${}^5\hat{E}$ and ${}^5\hat{B}_1$ are only allowed for $E_\perp$, and are shown in Figs. 19(a) and 19(b). The ${}^5\hat{B}_2\rightarrow{}^5\hat{E}$ transitions are allowed in first order, and $P=\frac{1}{16}$ in Fig. 19(a). The ${}^5\hat{B}_2\rightarrow{}^5\hat{B}_1$ transitions are forbidden in first order, and only become allowed by the spin-orbit mixing of the orbital ${}^5\hat{E}$ wave functions into both the ${}^5\hat{B}_2$ and ${}^5\hat{B}_1$ states. The result is a reduction factor $R$ which tells how much weaker than unity the transitions to ${}^5\hat{B}_1$ are [see Fig. 19(b)]. This factor is given by

$$R=\tfrac{3}{8}[\lambda(\mathcal{E}_2-2\mathcal{E}_1)/\mathcal{E}_1(\mathcal{E}_2-\mathcal{E}_1)]^2 \tag{37}$$

and is of the order of $R\sim 10^{-4}$ for ZnSe. Note that $R$ is zero when $\mathcal{E}_2=2\mathcal{E}_1$.

The $E_\perp$-type transitions of ${}^5\hat{B}_2\rightarrow{}^5\hat{A}_1$ are also weak and are comparable in intensity to the $E_\perp$-type

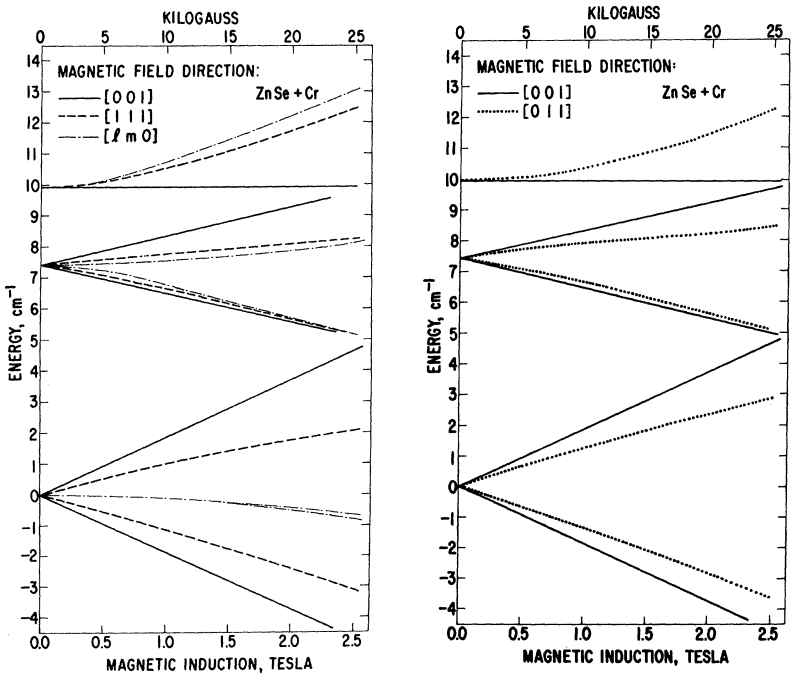


FIG. 18. (a) Splittings of the energy levels of the $^5\hat{B}_2$ ground-state manifold of $Cr^{2+}$ in ZnSe in an applied magnetic field. The three field directions are with respect to a $Cr^{2+}$ center aligned along [001]. The results for **B** along [111] are applicable to all four ⟨111⟩ directions. The notation [$lm$0] means **B** lies in the $xy$ plane. (b) Same as (a) except the magnetic fields are along [100] or [011]. The results for **B** along [101] are the same as [011].

$^5B_2 \rightarrow {}^5\hat{B}_1$ transitions. These are not shown in Fig. 19 because the $E_{||}$-type $^5\hat{B}_2 \rightarrow {}^5\hat{A}_1$ transitions are very strong, and are of order unity. They are, therefore, the strongest of all the electric dipole transitions from the ground state, and will mask any $E_\perp$-type $^5\hat{B}_2 \rightarrow {}^5\hat{A}_1$ transitions. Thus the most intense absorption band of $Cr^{2+}$ will be the $^5\hat{B}_2 \rightarrow {}^5\hat{A}_1$ transition for $E_{||}$ if any of the four models A, B, D, or E represents the correct model for the system.

### G. Optical Transitions: Model C

If $V_2 \simeq 0$ in Eq. (16), we have model C, in which the $E$ orbital state does not split under the $Q_\theta$, $Q_\epsilon$ distortion. In this case the final state for the optical

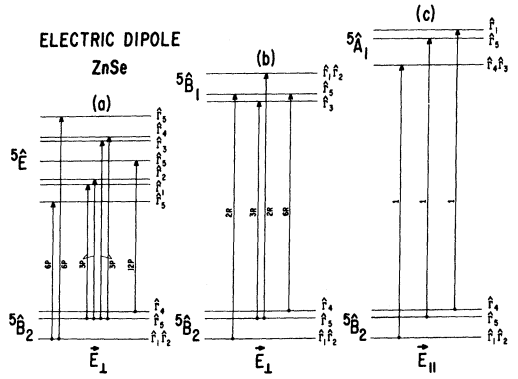


FIG. 19. Allowed electric dipole optical transitions of $Cr^{2+}$ in ZnSe in the infrared for models A, B, D, or E (see Fig. 16). The two cases for the electric vector of the plane-polarized light parallel or perpendicular to the [001] distortion axis of the center are considered. The relative intensities REI of the transition are given by the numbers on the vertical arrows. The $^5\hat{B}_2$-to-$^5\hat{A}_1$ transitions are the most intense, and are assumed to have unit strength. The reduction factor $R$ is given in Eq. (37), $P = \frac{1}{16}$.

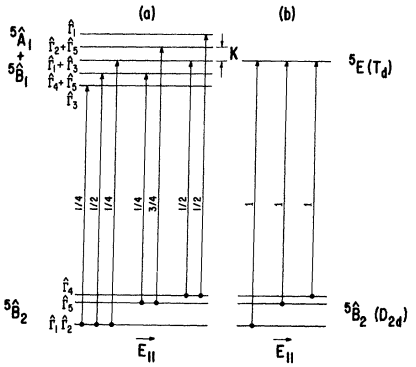


FIG. 20. Allowed electric dipole optical transitions of $Cr^{2+}$ in ZnSe in the infrared for model C (see Fig. 16). The only strong transitions are for the electric vector of the plane-polarized light parallel to the [001] distortion axis of the center. The relative intensities REI of the transitions are given by the numbers on the vertical arrows. Case (a) is when the $K(^5E)$ splitting of the $^5E$ orbital state is observable. Case (b) is when $K(^5E)$ is too small to be resolved experimentally.

transitions possesses $T_d$ symmetry. The three possible ground states with distortion axes [100], [010], and [001] are each ${}^5\hat{B}_2$ of $D_{2d}$. When these three are combined as a degenerate triplet, this triplet also possesses $T_d$ symmetry. In Fig. 20(a) we have chosen to label the levels by the irreducible representations of $D_{2d}$. We realize that the ${}^5\hat{A}_1$ and ${}^5\hat{B}_1$ wave functions are inseparably mixed in the upper state. The only strong optical transitions are for $E_{||}$, as shown in Fig. 20(a). In a macroscopic, unstrained crystal only $\frac{1}{3}$ of the $Cr^{2+}$ centers will be aligned with their distortion axis along [001]. Hence we will see absorption only from these, since in the polarized light the other centers will appear to have $E_\perp$, and the $E_\perp$ transitions are about $R$ or $10^{-4}$ times weaker. The five levels of the ${}^5E$ state are all equally spaced by an amount $K({}^5E)$ given by Eq. (8). This expression for $K({}^5E)$ is only strictly valid if $V_2=0$. If $|V_1| \gg |V_2| > 0$ such that $|V_2|$ is comparable in magnitude to the phonon energies of the host lattice, then we are in the dynamic Jahn-Teller regime.[38] Then $K({}^5E)$ is replaced by $K'({}^5E)$ given by

$$K'({}^5E) \approx \tfrac{1}{2}K({}^5E)\{1+\exp[-4\mathcal{E}_{JT}({}^5E)/\hbar\omega]\}. \quad (38)$$

See Eq. (4.24) of Ref. 15 for $K'({}^5E)$. Now if $K({}^5E)$ or $K'({}^5E)$ is much smaller than the resolution of our spectrometer, or if $K({}^5E)=0$ because $\rho=\lambda^2/\Delta$ in Eq. (8), then we have the situation shown in Fig. 20(b). Notice the similarity to Fig. 19(c). If $D({}^5\hat{A}_1)=0$ in Eq. (30), then Figs. 19(c) and 20(b) are identical.

### H. Zero-Phonon-Line Energies and Intensities

The models of Eq. (16) for the $Cr^{2+}$ center predict different structures for the optical-absorption band. Following the arguments of Sturge[39] and his Figs. 30 and 31(a), the models of Eq. (16) and Fig. 16 give

$$\bar{\nu}(\mathrm{ZPL}) = \Delta + [1-(V_2/V_1)^2]\mathcal{E}_{JT}({}^5T_2),$$
$$\bar{\nu}(\mathrm{peak}) - \bar{\nu}(\mathrm{ZPL}) = [1+(V_2/V_1)]^2\mathcal{E}_{JT}({}^5T_2). \quad (39)$$

The results of Eq. (39) for the various models are given in Table VI. The relative strength ZR of the ZPL is also different for the various models [see Eq. (3)]. The theoretical values of ZR for models A, C, and E are given by

$$\text{model A:}\quad \mathrm{ZR} \cong \tfrac{1}{64}(2/\pi)^{1/2}[\mathcal{E}_p/\mathcal{E}_{JT}({}^5T_2)]^{5/2},$$
$$\text{model C:}\quad \mathrm{ZR} = \exp[-\mathcal{E}_{JT}({}^5T_2)/\mathcal{E}_p], \quad (40)$$
$$\text{model E:}\quad \mathrm{ZR} \cong 1.$$

Models B and D give intermediate values of ZR. In Eq. (40) the quantity $\mathcal{E}_p$ is a characteristic phonon energy. The expression in Eq. (40) for model A was derived by Ham[81] by assuming that all of the optical transitions are from the ground state of ${}^5\hat{B}_2$ to the several (unresolved) levels of ${}^5\hat{A}_1$ (see Figs. 15 and 16). Explicit account was taken of the energy versus $q_\theta$, $q_\epsilon$ curves from Sturge[39] (see his Figs. 6 and 20). The ZR value comes from the wave-function overlap between the lowest vibronic state[38] of ${}^5\hat{B}_2$ and the lowest vibronic state of ${}^5\hat{A}_1$. The expression in Eq. (40) for model C is the special case for $n=0$ of the formula[39,82] for the relative intensities of the phonon sidebands involving a number $n$ of phonons of average energy $\mathcal{E}_p$, i.e.,

$$I(n) = (1/n!)\,(\mathcal{E}/\mathcal{E}_p)^n \exp(-\mathcal{E}/\mathcal{E}_p), \quad (41)$$

where $\mathcal{E}=\mathcal{E}_{JT}({}^5T_2)$. The expression in Eq. (40) for model E is based on the observation that in model E the equilibrium position in $q_\theta$, $q_\epsilon$ space is the same for the ${}^5\hat{B}_2$ and the ${}^5\hat{A}_1$ states. Hence the wave-function overlap is a maximum, and there are no phonons or vibronic excitations involved in the transition. The whole optical intensity is in the ZPL in this special case.

TABLE VI. Some properties of the zero-phonon line of $Cr^{2+}$ in II-VI compounds for various models of the center, from Eq. (39).

| Model[a] | $V_2/V_1$ | $\bar{\nu}$(ZPL)[b] | $\bar{\nu}$(peak) − $\bar{\nu}$(ZPL)[b] |
|---|---|---|---|
| A | +1 | $\Delta$ | 4.00$\mathcal{E}$ |
| B | +¼ | $\Delta$+0.94$\mathcal{E}$ | 1.56$\mathcal{E}$ |
| C | 0 | $\Delta$+$\mathcal{E}$ | 1.00$\mathcal{E}$ |
| D | −¼ | $\Delta$+0.94$\mathcal{E}$ | 0.56$\mathcal{E}$ |
| E | −1 | $\Delta$ | 0 |

[a] See Eq. (16).
[b] $\mathcal{E}=\mathcal{E}_{JT}({}^5T_2)$.

## VII. ANALYSIS OF RESULTS

### A. General

In all of the cubic(zinc-blende) structure crystals studied the ${}^5T_2$- to -${}^5E$ absorption band at 2°K looks about the same (see Fig. 2). The absorption peak at 2°K shifts from $\bar{\nu}=5800$ cm$^{-1}$ in cubic ZnS to $\bar{\nu}=5170$ cm$^{-1}$ in CdTe. There are some differences in the relative strength of the ZPL and in the prominence of phonon structure in the phonon-assisted region (see Fig. 2). The total oscillator strength $f$ of the $Cr^{2+}$ band is comparable to that found previously[15] for $Fe^{2+}$ in these crystals. This magnitude for the oscillator strength means that we are studying an electric dipole transition in the $Cr^{2+}$ center, as we also were for the $Fe^{2+}$ center. The models of Figs. 14, 15, 19, and 20 all predict such allowed transitions from the ground state; hence we cannot yet decide just from the optical results between $T_d$ and $D_{2d}$ site symmetry from the $Cr^{2+}$. If the symmetry is $T_d$, the transition at 4°K is $\Gamma_1({}^5T_2)\rightarrow\Gamma_5({}^5E)$ (see Fig. 14). If the symmetry is $D_{2d}$, then in models A, B, D, and E the transitions are $\hat{\Gamma}_1\hat{\Gamma}_2({}^5\hat{B}_2)\rightarrow\hat{\Gamma}_3\hat{\Gamma}_4({}^5\hat{A}_1)$ (see Figs. 15, 16, and 19). For model C the transitions are

TABLE VII. Values of $\Delta$, $\mathcal{E}_{JT}(^5T_2)$, and $\mathcal{E}_p$ derived from the application of Eqs. (39) and (40) to the near-infrared results in Table I.

| Model | Crystal | $\Delta$ ($cm^{-1}$) | $\mathcal{E}_{JT}(^5T_2)$ ($cm^{-1}$) | $\mathcal{E}_p$ ($cm^{-1}$) |
|---|---|---|---|---|
| A | Cubic ZnS | 5224 | 144 | 66 |
| | ZnSe | 4975 | 138 | 34 |
| | ZnTe | 4994 | 134 | 36 |
| | CdS | 4686 | 154 | 23 |
| | CdTe | 4700 | 118 | $<17$ |
| C | Cubic ZnS | 4650 | 575 | 91 |
| | ZnSe | 4425 | 550 | 69 |
| | ZnTe | 4460 | 535 | 67 |
| | CdS | 4070 | 615 | 68 |
| | CdTe | 4230 | 470 | $<50$ |

$\hat{\Gamma}_1\hat{\Gamma}_2(^5\hat{B}_2)\rightarrow\hat{\Gamma}_3\hat{\Gamma}_4(^5\hat{A}_1+^5\hat{B}_1)$ (see Fig. 20). We now make the assumption that the near-infrared, far-infrared, and ESR observations all refer to the same type of $Cr^{2+}$ center.

### B. Model for $Cr^{2+}$ Center

We conclude that the $Cr^{2+}$ center does not have the $^5T_2$ ground-state structure shown in Fig. 14 based on both the far-infrared[7] and ESR[40–43] results. Thus we have introduced a static Jahn-Teller distortion in Sec. VI. C, and have proposed five different models for the center based on the ratio $V_2/V_1$ [see Eq. (16)]. We shall try to select the most appropriate of these models based on the comparison of theoretical and experimental values for $\Delta$, ZR, $\mathcal{E}_{JT}$, and $\mathcal{E}_p$.

### C. Value of $\Delta$

The cubic-crystal-field model of Sec. VI B predicts that the $^5T_2$ and $^5E$ components of the $^5D$ free-ion state will be split by an amount $\Delta$ when the $Cr^{2+}$ ion is placed in an undistorted tetrahedral site. However, the sites are distorted. To extract a value of $\Delta$ from the experimental results we have to specify the model in Eq. (16) or Table VI. If we neglect the second-order effects of $\mathcal{H}_{SO}$ and the first-order effects of $\mathcal{H}_{SS}$ which are of magnitude 10 $cm^{-1}$ or less in energy, then we have from Eq. (39) and Table VI

$$\Delta=\bar{\nu}(\mathrm{ZPL})-m\mathcal{E}_{JT}(^5T_2), \qquad 0\leq m\leq 1. \quad (42)$$

Since both $m$ and $\mathcal{E}_{JT}(^5T_2)$ depend on $V_2/V_1$, we have to make some preliminary evaluation of our five models. Clearly model E is not applicable, since in Eq. (40) it predicts that all of the optical intensity is in the ZPL, in disagreement with the results in Table I. The predictions of models B–D as to $\Delta$, ZR, $\mathcal{E}_{JT}$, and $\mathcal{E}_p$ will all be fairly similar, and we will not be able to distinguish among them clearly. So we will use model C for our computations, but will realize that $V_2$ may be small compared to $V_1$ instead of identically zero. We can distinguish between models A and C. Thus we shall also compute various quantities for model A. The resultant values of $\Delta$ for models A and C are given in Table VII. For either model $4000<\Delta<5000$ $cm^{-1}$ for almost all of the crystals, and are 35–85% larger than the values for $Fe^{2+}$ (see Tables VII and VIII). These $Cr^{2+}$ values are about equal to the $\Delta$ values for $Mn^{2+}$ in these same crystals.[8–13]

### D. Value of $\mathcal{E}_{JT}$

An optically determined value of $\mathcal{E}_{JT}(^5T_2)$ can be obtained for models A and C from the quantity $\bar{\nu}(\mathrm{peak})-\bar{\nu}(\mathrm{ZPL})$ using Eq. (39) and Tables I and VI. These values are given in Table VII. For model A the derived values of $\mathcal{E}_{JT}(^5T_2)$ are comparable to the phonon energies for the crystals (see Tables II–IV and Ref. 51). For model C the derived values of $\mathcal{E}_{JT}(^5T_2)$ are 2 to 5 times larger than known phonon energies. For both models $\mathcal{E}_{JT}(^5T_2)\ll\Delta$. Following the arguments of Ham,[38] it is necessary that $\mathcal{E}_{JT}$ be significantly larger than the energies of the lattice phonons in order for the system to exhibit a static Jahn-Teller distortion. If $\mathcal{E}_{JT}$ is comparable to the phonon energies, then we are in the dynamic Jahn-Teller regime. This indicates that model C is in better agreement with the experimental result that $Cr^{2+}$ possesses a static Jahn-Teller distortion in the $^5T_2$ ground state.

### E. Value of $\mathcal{E}_p$

A value of $\mathcal{E}_p$ can be derived for each crystal from Eq. (40) and the experimental value of ZR. Again we do not consider model E and concentrate on models A and C. The derived values of $\mathcal{E}_p$ are given in Table VII. Notice that for model A the $\mathcal{E}_p$ values are noticeably less than some average phonon energy of the crystal, and in fact are less than the lowest peak in the phonon density of states at TA($L$) (see Tables II–IV). For model C the $\mathcal{E}_p$ values lie between the [TA($L$)] and [LA($X$) or LO($X$)] values for the crystal in question. This point will be treated more fully later. Therefore, the $\mathcal{E}_p$ values for model C appear to be more nearly those of an "average phonon" than those derived from model A. This is another reason why we prefer model C.

The third reason we prefer model C is that it has no static or dynamic Jahn-Teller splitting of the $^5E$ orbital state of $Cr^{2+}$ in $T_d$ symmetry. We have studied the analagous $^5E$ orbital state of $Fe^{2+}$ in $T_d$ symmetry,[15,16,18,20] and have not seen any evidence of static Jahn-Teller effects. There may be a weak dynamic effect[20] for $Fe^{2+}$ in CdTe. Thus in these cases $V_2\approx 0$ for $Fe^{2+}$. So we are inclined to believe $|V_2/V_1|\ll 1$ for $Cr^{2+}$. So based on the derived values of $\mathcal{E}_{JT}(^5T_2)$ and $\mathcal{E}_p$ for $Cr^{2+}$, and on the previous results for $Fe^{2+}$, we believe model C is the correct model for $Cr^{2+}$.

TABLE VIII. Comparison of experimental values of $\Delta$ and $f$ for the ${}^5T_2$-to-${}^5E$ absorption band of $Cr^{2+}$ ($3d^4$) and $Fe^{2+}$ ($3d^6$) in II-VI compounds at liquid-helium temperature. The $\Delta$ values for $Cr^{2+}$ are based on model C.

| Crystal[a] | $\Delta(Cr^{2+})$ ($cm^{-1}$) | $\Delta(Fe^{2+})$[b] ($cm^{-1}$) | $\frac{\Delta(Cr^{2+})}{\Delta(Fe^{2+})}$ | $f(Cr^{2+})$[c] | $f(Fe^{2+})$[c] |
|---|---|---|---|---|---|
| ZnS | 4650 | 3400[b] | 1.37 | 4[d] | 0.64[b] |
| ZnSe | 4425 | 3200[e] | 1.38 | 0.5 | ··· |
| ZnTe | 4460 | 2700[f] | 1.65 | ··· | ··· |
| CdS | 4070 | 3000[f] | 1.36 | 1.5[g] | ··· |
| CdTe | 4230 | 2480[b] | 1.71 | ··· | 0.36[h] |

[a] Cubic sphalerite structure except for CdS.
[b] $\Delta$ corresponds to approximately the center of the band (see Ref. 15).
[c] The true size of the oscillator strength $f$ is $10^{-3}$ times the value given in the table.
[d] Value for mixed-polytype ZnS (see Ref. 6).
[e] References 17 and 19.
[f] Reference 17.
[g] Reference 2.
[h] Corrected for actual amount of $Fe^{2+}$ in the sample (see Refs. 15 and 20).

Thus $V_2 \cong 0$, and $\mathcal{E}_{JT}({}^5E) \cong 0$. We cannot really rule out models B and D, where $V_2$ is finite but $|V_2/V_1| \ll 1$. Further work would be needed to make this decision. The above reasoning also explains why we have previously eliminated the case $|V_2| > |V_1|$.

We shall now proceed with the rest of the analysis of the results with the assumption that model C is the correct one.

### F. Value of $D$, $a$, and $g_{||}$

Now that we have values for $\lambda$, $\mathcal{E}_{JT}$, and $\Delta$, we can compute the expected value of $D({}^5\hat{B}_2)$ from Eq. (30). For this we use model C, where

$$\mathcal{E}_1 = 3\mathcal{E}_{JT}({}^5T_2),$$
$$\mathcal{E}_2 = \mathcal{E}_3 = \Delta + 2\mathcal{E}_{JT}({}^5T_2), \tag{43}$$

The results are given in Table IX. Note that in all cases the predicted value is negative, i.e., $D({}^5\hat{B}_2) < 0$. The agreement with the experimental values in Table V is reasonably good for ZnSe and CdS with regard to both the sign and magnitude of $D$. For ZnTe,[43] the order of magnitude is correct, but the experimental value is greater than zero, not less. The reason for this difference is not understood, but the difference is real. In ZnTe,[43] the ground state is the $\hat{\Gamma}_4$ level of ${}^5\hat{B}_2$, not the $\hat{\Gamma}_1$, $\hat{\Gamma}_2$ level. For ZnS, the near-infrared results give $\bar{\nu} = 6.0\ cm^{-1} = 3.0\,|D|$; thus $|D| \cong 2\ cm^{-1}$, in good agreement with the magnitude of 1.6 $cm^{-1}$ predicted in Table IX.

TABLE IX. Calculated splittings of the ${}^5\hat{B}_2$ ground state of $Cr^{2+}$ as derived from the near-infrared optical absorption using model C.

| Crystal[a] | $D$[b] ($cm^{-1}$) | $a$[c] ($cm^{-1}$) |
|---|---|---|
| ZnS | −1.60 | +0.055 |
| ZnSe | −1.62 | +0.061 |
| ZnTe | −1.56 | +0.065 |
| CdS | −1.97 | +0.052 |
| CdTe | −1.43 | +0.086 |

[a] All sphalerite structure except CdS, which is wurtzite.
[b] Computed from Eq. (30).
[c] Computed from Eq. (31).

The value of $a$ [see Eq. (31)] can also be computed. The computed value of $a$ is always positive. Since $a$ is independent of $D({}^5\hat{B}_2)$, then we should expect our calculation to be valid for ZnTe as well as ZnSe and CdS. From Tables V and IX we see that our calculation gives the correct sign for ZnTe and the correct magnitude, i.e., to within a factor of 3, for CdS, ZnSe, and ZnTe. Another experimental measure of $a$ is the linewidth of the far-infrared transition, i.e., $\hat{\Gamma}_1$, $\hat{\Gamma}_2 \rightarrow \hat{\Gamma}_4$. For ZnSe this occurs at $\bar{\nu} = 7.43\ cm^{-1}$, with an experimental linewidth of $\Delta\bar{\nu} = 0.04\ cm^{-1}$. Since magnetic dipole optical transitions are allowed to $\hat{\Gamma}_4$ from both $\hat{\Gamma}_1$ and $\hat{\Gamma}_2$, we should expect $\Delta\bar{\nu} \geq a$. The experimental $\Delta\bar{\nu}$ for ZnSe is comparable to both the measured value of $|a| = 0.024\ cm^{-1}$ from ESR and the computed value of $a = +0.062\ cm^{-1}$. The experimental fact that $\Delta\bar{\nu}$ is not much larger than $a$ means that there is not much inhomogeneous broadening of the levels involved. This means that $\mathcal{E}_1$ and $\mathcal{E}_3$ are the same from $Cr^{2+}$ site to $Cr^{2+}$ site to within $\pm\frac{1}{4}\%$, which seems like a reasonable limit for the effect of small random strains.

The values of $g_{||}$ can be computed from Eq. (34). These values are nearly the same for all of the crystals studied, and are

$$g_{||}(\hat{\Gamma}_1\hat{\Gamma}_2) = 7.56 \pm 0.08,$$
$$g_{||}(\hat{\Gamma}_5) = 3.78 \pm 0.04. \tag{44}$$

The limits in Eq. (44) indicate the variations caused by variations in $\Delta$. From comparison with Table V we see the computation gives values close to, but slightly less than, the experimental ones.

### G. Zero-Phonon Lines in Near Infrared

For a crystal temperature of 2°K a maximum of one ZPL was observed in the near-infrared region near

TABLE X. Energies in wave numbers ($cm^{-1}$) of $E$-mode phonons in various II-VI compounds.

| Lattice mode | ZnS (cubic) | ZnSe | ZnTe | CdS | CdTe |
|---|---|---|---|---|---|
| TA($L$) | 72 | 49 | 42 | 35 | 28 |
| LA($X$) | ··· | ~185 | ~150 | ··· | ? |
| LO($X$) | 304 | ··· | ··· | ? | ··· |
| TO($L$) | 342 | ~250 | ? | ? | ? |

$\bar{\nu}=5000$ $cm^{-1}$ for each of the cubic crystals (see Fig. 3). Do the two models A and C differ in their predictions of the ZPL structure? Model A as well as models B, D, and E predict that the $\mathcal{E}(^5\hat{A}_1)-\mathcal{E}(^5\hat{B}_1)$ splitting is larger than $|D(^5\hat{A}_1)|$ or $|D(^5\hat{B}_1)|$. Hence the strong electric dipole transitions for the ZPL in the near infrared will be those shown in Fig. 19(c). The value of $D(^5\hat{A}_1)$ from Eq. (30) is

$$D(^5\hat{A}_1)=-1.6 \text{ to } -1.9 \text{ cm}^{-1} \quad (45)$$

for all five crystals studied. Hence $|3D|$, the second-order spin-orbit and spin-spin splitting in the $^5\hat{A}_1$ state, is comparable to or less than the observed ZPL linewidth in Table I. This means the structure of the $^5\hat{A}_1$ state should not be resolvable. Our experimental resolution of the spectrometer was 1.5 $cm^{-1}$, so the linewidth is due to the crystal, not the apparatus. If model C is correct, then $\mathcal{E}(^5\hat{A}_1)-\mathcal{E}(^5\hat{B}_1)$ is zero. In this limit the ZPL transitions will be those of Fig. 20(a). From Eq. (8) we see that $K(^5E)$ is

$$K(^5E)=2.5 \text{ to } 2.9 \text{ cm}^{-1} \quad (46)$$

for all of the crystals studied. Comparing 2K [see Fig. 20(a)] with the observed ZPL linewidths, we conclude that this splitting is also unobservable. This means that $2K'(^5E)$ from Eq. (38) would also be unobservable. Hence, we cannot find any evidence from the structure of the ZPL that will allow us to decide between models A, B, C, D, or E. Thus for any of the models the picture of Fig. 20(b) is useful for showing that only one ZPL is expected at 2°K, and one or two more ZPL should appear at slightly lower values of $\bar{\nu}$ at temperatures where $kT\cong 3.5\,|D(^5\hat{B}_2)|$. Since $\mathcal{E}(\hat{\Gamma}_4, {}^5\hat{B}_2)-\mathcal{E}(\hat{\Gamma}_5, {}^5\hat{B}_2)=|D|$, and since $|D|$ is less than the ZPL linewidth, we do not expect to resolve this splitting. Hence only one "hot" line at an energy of about $3.5\,|D|$ below the main ZPL should be observed. Such a line is seen for $Cr^{2+}$ in ZnS (see Sec. III B) and for $Cr^{2+}$ in ZnSe at 15°K (see Fig. 7). For ZnS and ZnSe the $\Delta\bar{\nu}$ energy differences are $6.0\pm0.3$ and $7\pm1$ $cm^{-1}$, respectively, below the main ZPL. In ZnSe the relative intensities of the "hot" line at $\bar{\nu}=4968$ $cm^{-1}$ and the main ZPL at $\bar{\nu}=4975$ $cm^{-1}$ and their changes in intensity with temperature are in reasonable agreement with Fig. 20(b).

From Fig. 19(a) and Table VII we would expect to see the $^5\hat{B}_2\rightarrow{}^5\hat{E}$ optical transitions at $\bar{\nu}\sim3\mathcal{E}_{JT}(5T_2)$ or about $\bar{\nu}=1600$ $cm^{-1}$. No such absorption band was seen in $Cr^{2+}$-doped ZnSe at 300°K, the only crystal studied in this wave-number region. Further work in this region of the spectrum at lower temperatures might be useful.

### H. Phonon-Assisted Transitions in Near Infrared

The phonon-assisted transitions make up the major fraction of the integrated optical intensity of the $\bar{\nu}\sim5000$ $cm^{-1}$ band in the near infrared (see Fig. 2). The general shape of this band can be computed from Eq. (41) using the values of $\mathcal{E}_p$ in Table VII. The results of such a calculation based on model C are shown in Fig. 2 for ZnSe. The agreement with the observations is considered to be reasonable. However, we note that the detailed structure of the band shown in Fig. 2 for ZnS and in Fig. 3 for three other crystals is not reproduced by this model. It is clear that there are really several different phonons that are coupled with the $Cr^{2+}$ center. The energies and tentative identifications of these phonons are given in Table II. Consider the TA($L$) phonons. It is possible[83] to construct from a suitable linear combination of TA($L$) phonons that are traveling in the four equivalent ⟨111⟩ directions in $k$ space a vibrational mode of $E$ character around a Zn site in ZnSe. It is also possible to do this for LA($X$) phonons at the $X$ critical point. Such phonons we shall, for present purposes, call $E$-mode phonons. These $E$-mode phonons are[67] TA($L$), LO($X$), and TO($L$) for ZnS and TA($L$), LA($X$), and TO($L$) for ZnSe, ZnTe, and CdTe. The switch from LO($X$) to LA($X$) in the two cases depends on whether the cations or anions of the host lattice are more massive. The phonon energies at these various critical points are given in Table X. The ZnS values are from a neutron scattering study.[51] The TA($L$) value for ZnSe is from Table IV, while the TO($L$) value is an educated guess. The TA($L$) values for ZnTe, CdS, and CdTe and the LA($X$) values for ZnSe and ZnTe are based on some unpublished work[83] in which the two-phonon optical absorption peaks in the far infrared have been measured and correlated with neutron scattering data and known elastic constants. The general agreement of the phonon energies in Tables II and X indicates that the $E$-mode phonons are the ones which couple to the $Cr^{2+}$ centers. Furthermore, the $\mathcal{E}_p$ value in Table VII for model C is in all cases

$$\text{TA}(L)<\mathcal{E}_p<\text{LA}(X) \quad \text{or} \quad \text{LO}(X). \quad (47)$$

Thus $\mathcal{E}_p$ represents some average energy of the $E$-mode phonons involved in the phonon-assisted transitions.

### I. Zero-Phonon Lines in Far Infrared

The far-infrared absorption of ZnSe both pure and doped with $Cr^{2+}$ or $Mn^{2+}$ is given in Fig. 12. The

energies for the various peaks are listed in Table IV together with our tentative identification. This identification is based primarily on some unpublished work[83] concerning phonon energies at critical points. We see that the narrow line at $\bar{\nu}=7.43\pm0.02$ cm$^{-1}$ is an electronic transition of the $Cr^{2+}$, while all the other structures are related to lattice phonons of ZnSe. The experimental oscillator strength of this 7.43-cm$^{-1}$ line is $f=1.3\times10^{-9}$. If we use the undistorted model for $Cr^{2+}$ as shown in Fig. 14, we would predict a magnetic dipole absorption line at $2K(^5T_2)=15.6$ cm$^{-1}$ and an electric dipole line at $3.6K(^5T_2)=26.3$ cm$^{-1}$, both with oscillator strengths $f\simeq10^{-9}$ [see Eq. (8)]. This is not what we see, and so on this basis, plus the fact that Fig. 14 does not fit the ESR results or the near-infrared optical results, we have rejected it.

If we next use models A, B, C, D, or E of Fig. 16, we get only a single allowed magnetic dipole transition from the $\hat{\Gamma}_1\hat{\Gamma}_2$ ground state to $\hat{\Gamma}_5$, with a computed[16] $f=1.6\times10^{-9}$ (see Fig. 17 for $B_z=0$). In order to compute $f$ we need to know the index of refraction of ZnSe in the far infrared. This was measured at 4.2°K by an interference-fringe counting technique in transmission on a polished slab of high-purity ZnSe. The results are

$$n=2.964+1.35\times10^{-5}(\bar{\nu})^2\pm0.25\% \qquad (48)$$

for $10<\bar{\nu}<90$ cm$^{-1}$. These results are in good agreement with Berlincourt *et al.*[84] at 298°K and Mitra[66] at 300°K, who obtain $n=3.03$ for $\bar{\nu}=0$. The values given by Aven *et al.*[65] and Manabe *et al.*[85] are too low, while Hadni *et al.*[86] give too large a value. The electric dipole transitions in these models are extremely weak ($f\sim10^{-11}$), and would not be seen. The calculated energy for this $\hat{\Gamma}_1\hat{\Gamma}_2$- to -$\hat{\Gamma}_5$ transition is just $\bar{\nu}=3\mid D\mid=4.83$ cm$^{-1}$ for ZnSe using Eq. (30). Allowing for some uncertainty in $D$, we believe that the observed $\bar{\nu}=7.43$ cm$^{-1}$ line is just this transition. Note also the good agreement between the computed and observed oscillator strengths. In computing $f$ we have been careful to take into account the fact that our $Cr^{2+}$ centers can have static distortions along any of the three ⟨100⟩ crystal axes.

If we have the correct model for the $Cr^{2+}$ center, then an external magnetic field will split the $^5\hat{B}_2$ levels as shown in Fig. 17 if the magnetic field is along the [001] axis of the center. This will be the case for only $\frac{1}{3}$ of the centers in any sample. Since there are three different ⟨100⟩ orientations, the other $\frac{2}{3}$ of the $Cr^{2+}$ centers will behave as if **B** were along [100] or [$lm$0] ,where $l$ and $m$ are integers [see Fig. 18(a)]. The absorption line will split into two components, one moving to higher and one to lower energy with increasing $B_z$. If the applied magnetic field is in a [011] direction, then it makes an angle of 45° with $\frac{2}{3}$ of the centers and an angle of 90° with $\frac{1}{3}$ of them. This was the case considered in Sec. IV B. The more populous orientation will be like the [011] field acting on [001] axis centers as shown in Figs. 18(b) and 13. The calculated and observed splittings of the 7.43-cm$^{-1}$ line are in good agreement in Fig. 13. Thus we have clearly established that this line is an electronic transition of the predicted nature, and is not a localized vibrational mode associated with the $Cr^{2+}$ impurity.

### J. Phonon Structure in Far Infrared

The optical absorption of pure ZnSe is shown in Fig. 12, and there are characteristic inflections in the curve at $\bar{\nu}=141$ and 176 cm$^{-1}$. The first of these, we believe, is a two-phonon absorption peak, and should correspond to a peak in the combined density-of-states curve, similar to Fig. 6 of Sennett *et al.*[87] By also taking in account the fact that the phonon spectrum of ZnSe should be similar to that of GaAs, which has been measured by neutron scattering,[88] we have arrived at the phonon assignments as given in Table IV. The $\bar{\nu}=176$ cm$^{-1}$ peak is probably a one-phonon peak where the absorption is allowed because of the presence of impurities or Zn and Se isotopes. The phonon energies in ZnSe turn out to be about 85% of the corresponding energies in GaAs. We note that the critical points in the Brillouin zone are those at $L$ and $X$ (see Bouckaert *et al.*[89]).

The presence of impurities in the lattice makes some of the one-phonon processes allowed.[67] In Fig. 12 it can be seen that the Cr impurity introduces an absorption peak at $\bar{\nu}=49$ cm$^{-1}$, while both the Cr and the Mn introduce absorption peaks at $\bar{\nu}=70.5$ and 96 cm$^{-1}$. Since from Fig. 15 we do not expect any electronic transitions of $Cr^{2+}$ at or near $\bar{\nu}=49$ cm$^{-1}$, and since we know from Table II that the $Cr^{2+}$ couples strongly to the $E$-mode part of the TA($L$) vibration at $\bar{\nu}=49$ cm$^{-1}$, we attribute this peak to an impurity-induced one-phonon TA($L$) absorption. The 70.5- and 96-cm$^{-1}$ bands are clearly not electronic transitions of the $Cr^{2+}$, since they are caused by both $Mn^{2+}$ and $Cr^{2+}$. These are assigned to the acoustic phonons[51,89] TA($X$) and $A_2(K)$. The $A_2(K)$ means the middle acoustic branch at the $K$ point. This is not really a TA phonon, since there is no well-defined transverse polarization here.

We conclude that the only electronic transition of $Cr^{2+}$ in ZnSe in the far infrared is at $\bar{\nu}=7.43$ cm$^{-1}$.

## VIII. POSSIBLE TRIGONAL DISTORTION

Since a tetrahedron has a $T_2$ normal mode, it is possible that the $Cr^{2+}$ center could distort along a ⟨111⟩ axis and give rise to a trigonal local field $C_{3v}$ (see Sec. VI C). Such a distortion is not compatible with the ESR results. We want to show here that it is not compatible with the far-infrared optical results either. This trigonal distortion will split the $T_2$ orbital ground state but not the $E$ orbital excited state. To this extent it is compatible with the optical data. The $C_{3v}$ distortion yields an orbital singlet $^5\tilde{A}_1$ ground state. This state is further split into three spin-orbit

levels $\tilde{\Gamma}_1+2\tilde{\Gamma}_3$. The tildes indicate irreducible representations of $C_{3v}$. The $\tilde{\Gamma}_1$ singlet is the ground state, since in this case $D>0$. This result is in contrast to the tetragonal distortion case, where the sign of $D$ is variable [see Eq. (30)]. The lower $\tilde{\Gamma}_3$ level lies somewhere between 3 and 10 $cm^{-1}$ above the $\tilde{\Gamma}_1$. There is only a single spin-allowed magnetic dipole optical transition from the $\tilde{\Gamma}_1$ ground state. This transition is to the lower $\tilde{\Gamma}_3$ level. The transition from $\tilde{\Gamma}_1$ to the second $\tilde{\Gamma}_3$ is spin forbidden. Thus we should see a single optical absorption line in the far infrared for $Cr^{2+}$ in this $C_{3v}$ site.

If we now apply a magnetic field along some chosen crystallographic direction, we can distinguish between $D_{2d}$ and $C_{3v}$ distorted sites. For a field in the [011] direction the $Cr^{2+}$ centers with distortion axes along [111] and [$\bar{1}$11] will show a splitting of the $\tilde{\Gamma}_1\rightarrow\tilde{\Gamma}_3$ transition which is linear in **B**. We obtain

$$\lim_{B\rightarrow 0}(\delta\mathcal{E}/\mu_B B)=\tfrac{4}{3}\sqrt{6}=3.27, \qquad (49)$$

where $\delta\mathcal{E}$ is the splitting in wave numbers. The other half of the $Cr^{2+}$ centers with distortion axes along [11$\bar{1}$] and [1$\bar{1}$1] will show only a splitting quadratic in **B**. The $Cr^{2+}$ centers in ZnSe with the $D_{2d}$ tetragonal distortion have a predicted splitting of

$$\lim_{B\rightarrow 0}(\delta\mathcal{E}/\mu_B B)=2\sqrt{2}=2.83. \qquad (50)$$

The observed splitting at low values of **B** in Fig. 13 is

$$\delta\mathcal{E}/\mu_B B=2.6,$$

which agrees rather better with the tetragonal distortion model of Eq. (50) and Fig. 13 than with the trigonal distortion prediction of Eq. (49).

Thus from the far-infrared optical results alone we can say the tetragonal $D_{2d}$ distortion of the $Cr^{2+}$ center is the preferred model, in agreement with the ESR result. There does not appear to be any way to decide between these two models from the near-infrared results.

## IX. CONCLUSIONS

Near- and far-infrared optical-absorption studies of levels derived from the $^5D$ free-ion state of $Cr^{2+}$ in several II-VI compounds can be explained by assuming that the $Cr^{2+}$ is substitutionally incorporated at a cation site. The $3d^4$ configuration of the $Cr^{2+}$ ion leads to a tetragonal compression of the site along a ⟨100⟩ axis, yielding a $D_{2d}$ symmetry in the ground-state manifold. The ground state is then $^5\hat{B}_2$. In the excited state, $^5\hat{A}_1+{}^5\hat{B}_1$, or $^5E$, most if not all of this distortion appears to relax and the site returns to a $T_d$ symmetry. These experiments allow us to derive values for the Jahn-Teller energy in the ground state, $\mathcal{E}_{JT}(^5T_2)$, which is of the order of 500 $cm^{-1}$ for all five crystals studied. The value of $\mathcal{E}_{JT}$ ($^5E$) is very much smaller or possibly zero. The observations are in agreement with ESR experiments on $Cr^{2+}$ in the II-VI compounds, and yield reasonable predictions for the electron-spin-resonance parameters $D$, $a$, $g_{\|}$, and $g_{\perp}$.

The $Cr^{2+}$ centers, which undergo an $E$-type distortion in the ground state, exhibit coupling mainly to $E$-mode phonons in the phonon-assisted optical transitions. The average energy of the phonons to which the $Cr^{2+}$ centers couple is $\mathcal{E}_p\simeq 70$ $cm^{-1}$, which is in reasonable agreement with a more detailed analysis of the phonon spectrum of the crystals.

## ACKNOWLEDGMENTS

The authors wish to thank F. S. Ham for many helpful discussions in the course of this work and G. D. Watkins for permission to quote some results of his ESR studies on $Cr^{2+}$ in ZnTe prior to publication. We wish to thank R. Lewandowski for his assistance in the preparation of several samples. Thanks are also extended to C. S. Kelley and F. E. Williams for reports of their work prior to publication on the $Cr^{2+}$ optical absorption in ZnS,[90] and to D. Langer for a sample of Mn-doped ZnSe.

---

* Harkness Fellow, on leave from Atomic Energy Research Establishment, Harwell, Didcot, Berkshire, United Kingdom, now returned.

† Work supported in part by the Advanced Research Projects Agency through the Materials Science Center, Cornell University, Ithaca, N.Y.

[1] R. K. Watts, Phys. Letters **27A,** 469 (1968).
[2] R. Pappalardo and R. E. Dietz, Phys. Rev. **123,** 1888 (1961).
[3] J. W. Allen, Physica **29,** 764 (1963).
[4] W. E. Hagston, J. Phys. C **1,** 818 (1968).
[5] C. S. Kelley, R. B. Lauer, and F. E. Williams, Bull. Am. Phys. Soc. **11,** 85 (1966).
[6] C. S. Kelley and F. E. Williams, Bull. Am. Phys. Soc. **13,** 726 (1968).
[7] J. T. Vallin, G. A. Slack, S. Roberts, and A. E. Hughes, Solid State Commun. **7,** 1211 (1969).
[8] D. S. McClure, J. Chem. Phys. **39,** 2850 (1963).
[9] A. I. Ryskin, G. I. Khilko, B. I. Maksakov, and K. K. Dubenskii, Opt. i Spektroskopiya **16,** 274 (1964) [Opt. Spectry. (USSR) **16,** 149 (1964)].
[10] D. Langer and S. Ibuki, Phys. Rev. **138,** A809 (1965).
[11] D. Langer and H. J. Richter, Phys. Rev. **146,** 554 (1966).
[12] H. E. Gumlich, R. L. Pfrogner, J. C. Shaffer, and F. E. Williams, J. Chem. Phys. **44,** 3929 (1966).
[13] M. Ikeda, K. Itoh, and H. Sato, J. Phys. Soc. Japan **25,** 455 (1968).
[14] W. Low and M. Weger, Phys. Rev. **118,** 1130 (1960).
[15] G. A. Slack, F. S. Ham, and R. M. Chrenko, Phys. Rev. **152,** 376 (1966).
[16] G. A. Slack, S. Roberts, and F. S. Ham, Phys. Rev. **155,** 170 (1967).
[17] J. M. Baranowski, J. W. Allen, and G. L. Pearson, Phys. Rev. **160,** 627 (1967).
[18] G. A. Slack and B. M. O'Meara, Phys. Rev. **163,** 335 (1967).
[19] J. H. Haanstra, in *II-VI Semiconducting Compounds*, edited by D. G. Thomas (Benjamin, New York, 1967), p. 207.
[20] G. A. Slack, S. Roberts, and J. T. Vallin, Phys. Rev. **187,** 511 (1969).
[21] R. Pappalardo, D. L. Wood, and R. C. Linares, J. Chem. Phys. **35,** 2041 (1961).

[22] H. A. Weakliem, J. Chem. Phys. **36,** 2117 (1962).
[23] K. K. Dubenskii, Ya. E. Kariss, A. I. Ryskin, P. P. Feofilov, and G. I. Khilko, Opt. i Spektroskopiya **19,** 635 (1965) [Opt. Spectry. (USSR) **19,** 353 (1965)].
[24] D. H. Loescher, J. W. Allen, and G. L. Pearson, J. Phys. Soc. Japan Suppl. **21,** 239 (1966).
[25] M. L. Reynolds, W. E. Hagston, and G. F. J. Garlick, Infrared Phys. **7,** 211 (1967).
[26] R. S. Anderson, Phys. Rev. **164,** 398 (1967).
[27] R. Pappalardo, D. L. Wood, and R. C. Linares, J. Chem. Phys. **35,** 1471 (1961).
[28] M. L. Reynolds and G. F. J. Garlick, Infrared Phys. **7,** 151 (1967).
[29] J. M. Baranowski, J. W. Allen, and G. L. Pearson, Phys. Rev. **167,** 758 (1968).
[30] J. L. Birman, Phys. Rev. **121,** 144 (1961).
[31] R. Pappalardo, J. Mol. Spectry. **6,** 554 (1961).
[32] R. E. Dietz, H. Kamimura, M. D. Sturge, and A. Yariv, Phys. Rev. **132,** 1559 (1963).
[33] I. Broser, H. Maier, and H. J. Schulz, Phys. Rev. **140,** A2135 (1965).
[34] I. Broser and H. Maier, J. Phys. Soc. Japan Suppl. **21,** 254 (1966).
[35] W. E. Hagston, J. Phys. C **1,** 810 (1968).
[36] J. S. Griffith, *The Theory of Transition Metal Ions* (Cambridge U. P., Cambridge, England, 1961).
[37] M. T. Hutchings, in *Solid State Physics*, edited by F. Seitz and D. Turnbull (Academic, New York, 1965), Vol. **16,** p. 227.
[38] F. S. Ham, Phys. Rev. **138,** A1727 (1965); **166,** 307 (1968); in *Electron Paramagnetic Resonance*, edited by S. Geschwind (Plenum, New York, 1970).
[39] M. D. Sturge, in *Solid State Physics*, edited by F. Seitz, D. Turnbull, and H. Ehrenreich (Academic, New York, 1967), Vol. 20, p. 91.
[40] T. L. Estle, G. K. Walters, and M. DeWit, in *Paramagnetic Resonance*, edited by W. Low (Academic, New York, 1963), Vol. 1, p. 144.
[41] K. Morigaki, J. Phys. Soc. Japan **19,** 187 (1964).
[42] M. DeWit, A. R. Reinberg, W. C. Holton, and T. L. Estle, Bull. Am. Phys. Soc. **10,** 329 (1965); T. L. Estle and W. C. Holton, Phys. Rev. **150,** 159 (1966).
[43] G. D. Watkins (private communication) (ESR on $Cr^{2+}$ in ZnTe).
[44] Eagle-Picher Industries, Inc., Miami, Okla.
[45] F. K. Heumann, J. Electrochem. Soc. **109,** 345 (1962).
[46] I. G. Nolt, R. D. Kirby, C. D. Lytle, and A. J. Sievers, Appl. Opt. **8,** 309 (1969).
[47] S. Roberts and D. D. Coon, J. Opt. Soc. Am. **52,** 1023 (1962).
[48] Beckman Instruments, Inc., Fullerton, Calif.
[49] Applied Physics Corporation, Monrovia, Calif.
[50] C. E. Moore, *Atomic Energy Levels*, Natl. Bur. Std. (U.S.) Circ. No. 467 (U.S. Government Printing and Publishing Office, Washington, D. C., 1952), Vol. 2.
[51] L. A. Feldkamp, G. Venkataraman, and J. S. King, Solid State Commun. **7,** 1571 (1969).
[52] J. Dielemann, R. S. Title, and W. V. Smith, Phys. Letters **1,** 334 (1962).
[53] G. W. Ludwig and M. R. Lorenz, Phys. Rev. **131,** 601 (1963).
[54] R. S. Title, Phys. Rev. **131,** 623 (1963).
[55] R. S. Title, Phys. Rev. **133,** A1613 (1964).
[56] T. L. Estle and W. C. Holton, Bull. Am. Phys. Soc. **10,** 57 (1965).
[57] H. D. Fair, R. D. Ewing, and F. E. Williams, Phys. Rev. **144,** 298 (1966).
[58] K. Suto and M. Aoki, J. Phys. Soc. Japan **22,** 149 (1967).
[59] K. Suto, M. Aoki, M. Nakada, and S. Ibuki, J. Phys. Soc. Japan **22,** 1121 (1967).
[60] T. Taki and H. Bō, J. Phys. Soc. Japan **23,** 652 (1967).
[61] T. Taki and H. Bō, J. Phys. Soc. Japan **25,** 1324 (1968).
[62] P. B. Dorain and D. Locker, Bull. Am. Phys. Soc. **7,** 306 (1962).
[63] R. Rai, J. Y. Savard, and B. Tousignant, Phys. Letters **A25,** 443 (1967).
[64] F. Jellinke, Arkiv Kemi **20,** 447 (1963).
[65] M. Aven, D. T. F. Marple, and B. Segall, J. Appl. Phys. Suppl. **32,** 2261 (1960).
[66] S. S. Mitra, J. Phys. Soc. Japan Suppl. **21,** 61 (1966).
[67] R. Loudon, Proc. Phys. Soc. (London) **84,** 379 (1964).
[68] W. C. Ellis, Trans. AIME **188,** 886 (1950).
[69] E. Billig, J. Inst. Metals **83,** 53 (1954).
[70] E. U. Condon and G. H. Shortley, *The Theory of Atomic Spectra* (Cambridge U. P., London, 1935), p. 193.
[71] M. H. L. Pryce, Phys. Rev. **80,** 1107 (1950).
[72] R. E. Watson and M. Blume, Phys. Rev. **139,** A1209 (1965).
[73] R. E. Trees, Phys. Rev. **82,** 683 (1951).
[74] J. D. Dunitz and L. E. Orgel, J. Phys. Chem. Solids **3,** 20 (1957).
[75] C. J. Ballhausen, *Introduction to Liquid Field Theory* (McGraw-Hill, New York, 1962), p. 182.
[76] E. B. Tucker, Phys. Rev. **143,** 264 (1966).
[77] M. Tinkham, *Group Theory and Quantum Mechanics* (McGraw-Hill, New York, 1964).
[78] G. F. Koster, J. O. Dimmock, R. G. Wheeler, and H. Statz, *Properties of the Thirty-Two Point Groups* (MIT Press, Cambridge, Mass., 1963).
[79] There is a mistake in Table 35 on p. 46 of Ref. 78. In the $\hat{\Gamma}_3 \times \hat{\Gamma}_5$ matrix in the left-hand column of the second row the four entries read 0, 1, 1, 0 from top left to bottom right. They should read $-1, 0, 0, 1$.
[80] See Ref. 78, Table 84.
[81] F. S. Ham (private communication).
[82] E. O. Kane, Phys. Rev. **119,** 40 (1960). See also footnotes 84 and 85 of Ref. 15.
[83] G. A. Slack and S. Roberts (unpublished).
[84] D. Berlincourt, H. Jaffe, and L. R. Shiozawa, Phys. Rev. **129,** 1009 (1963).
[85] A. Manabe, A. Mitsuishi, and H. Yoshinaga, Japan. J. Appl. Phys. **6,** 593 (1967).
[86] A. Hadni, J. Claudel, and P. Strimer, Phys. Status Solidi **26,** 241 (1968).
[87] C. T. Sennett, D. R. Bosomworth, W. Hayes, and A. R. L. Spray, J. Phys. C **2,** 1137 (1969).
[88] J. L. T. Waugh and G. Dolling, Phys. Rev. **132,** 2410 (1963).
[89] L. P. Bouckaert, R. Smoluchowski, and E. Wigner, Phys. Rev. **50,** 58 (1936).
[90] C. S. Kelley and F. E. Williams, Phys. Rev. B **2,** 3 (1970).